Investigation of Heat Transfer and Distribution in the Core of Ghana Research Reactor-1 (GHARR-1) using STAR-CCM+ CFD Code

Salihu Mohammed

DEPARTMENT OF NUCLEAR ENGINEERING GRADUATE SCHOOL OF
NUCLEAR AND ALLIED SCIENCES COLLEGE OF BASIC AND APPLIED
SCIENCES UNIVERSITY OF GHANA

M.Phil

July, 2015

Investigation of Heat Transfer and Distribution in the core of Ghana Research Reactor-1 (GHARR-1) using STAR-CCM+ CFD Code

This thesis is submitted to the:

Department of NUCLEAR ENGINNERING COLLEGE OF BASIC AND APPLIED SCIENCES, UNIVERSITY OF GHANA

By

(Salihu Mohammed, 10391561)

BSc (Nigeria), 2005

In partial fulfilment of the requirements for the award of the degree of

MASTER OF PHILOSOPHY

In

NUCLEAR ENGINEERING

July, 2015

DECLARATION

This thesis is the result of work undertaken by Salihu Mohammed towards the award of Master of Philosophy in the Department of Nuclear Engineering, School of Nuclear and Allied Sciences, University of Ghana, under the Supervision of Dr. Vincent Yao Agbodemegbe and Dr. S. K. Debrah.

Salihu Mohammed

Date:

Vincent Yao Agbodemegbe, Ph.D.
(Principal Supervisor)
Date:

Seth Kofi Debrah, Ph.D.
(Co-Supervisor)
Date:

DEDICATION

To my truest love; Salmah Salihu Mohammed, Her Aunty; Talatu Salihu Galadima and her Grandmother; Ummulkhair Salihu Galadima.

ACKNOWLEDGEMENTS

First, I acknowledge Allah (S.W.T) for seeing me through the numerous hurdles that characterized my academic pursuit. I acknowledge the contributions of my supervisors Dr. S. K. Debrah and Dr. Vincent Yao Agbodemegbe. I also wish to specially acknowledge Emeritus Prof. E.H.K. Akaho and Dr. Emmanuel Ampomah-Amoako for their guidance throughout the programme. My acknowledgement also goes to the Staff of Nuclear Engineering Department, School of Nuclear and Allied Sciences (SNAS), Staff of Ghana Atomic Energy Commission (GAEC) especially Ghana Research Reactor-1 (GHARR-1) facility Engineer, Mr. Edward Oscar Amponsah-Abu, my friends and housemates at SNAS hostel especially Francis Siaw Nkansah and Lucky Woko for providing a power back-up used for the research simulations.

I wish to express my profound gratitude to the Chairperson, Niger State Polytechnic Board of Governing Council -Hajiya Dije Bala for helping me in getting the initial funding for this programme. I also owe a special acknowledgement to the sitting Rector of the Polytechnic at the time of my release for this study; Dr. Garba Kamaye Mohammed, the then Head of Basic and Applied Sciences Department; Late Mal. A. U. Abdulrashid. I also acknowledge my dear brother Adamu Salihu Rijau for always been there for me as a brother and a friend throughout my stay in Ghana. Garba Attah, Jamilu Umar Babuga, Aisha Mohammed Garo, Fatima Ogah, Tukur Mohammed Basey, Awwal Ibrahim Wushishi, Mal. Yahaya Zakari and Mal. Kasim I. Mohammed are also acknowledged.

I am also indebted to the following Organizations; Niger State Polytechnic, SNAS University of Ghana, Ghana Atomic Energy Commission, Rijau LGA Community and Developers of STAR-CCM+ (CD-ADAPCO).

TABLE OF CONTENTS

CHAPTER 3: METHODOLOGY

CHAPTER FIVE -CONCLUSION AND RECOMMENDATION

LIST OF TABLES

LIST OF FIGURES

NOMENCLATURE

Roman letters

x, y and z	direction of coordinates
D	dimension (s)
t	time
U, V and W	momentum components in x, y and z directions
P	Pressure
S	source term
G	productivity buoyancy
A	flow area
W	Inlet mass flow rate
K	turbulent kinetic energy
U, V and W	mass flow rates in x, y and z directions
A, B, C….	fuel rod positions
T	temperature
D, d	diameter
v	velocity
G	mass flux
Re.	Reynold’s
h	height
f	power peaking factor
Q	total power
q	segmental power

Greek Letters

ρ	density
ε	dissipation rate
τ	turbulent dissipation time-scale
Σ	summation
μ	dynamic viscosity
ϕ	heat flux

Subscripts

x, y, *and* z	direction components
b	buoyancy
in	inlet
s	surface
H	hydraulic
ith	position number
T	total

Abbreviations

STAR-CCM+	Simulation of Turbulent flow in Arbitrary Regions Computational Continuum Mechanics C++ based
MNSR	Miniature Neutron Source Reactors
CFD	Computational Fluid Dynamics
CAD	Computer-aided Design
CAE	Computer-aided Engineering
MATLAB	Matrix Laboratory
MAC	Marker and cell
COMSOL	Computer Solution
TRIGA IPR-R1	Training, Research, Isotopes, General Atomic.

NIST	National Institute of Standards and Technology
Exp.	Experimental
Sim.	Simulation
Avr.	Averaged
Out.	Outlet
Temp.	Temperature
Hot.	Hottest
Tke	Turbulent Kinetic Energy
Tdr	Turbulent Dissipation Rate
SAT	Surface Average Temperature
BAT	Bulk Average Temperature
BAD	Bulk Average Density
BADV	Bulk Average Dynamic Viscosity
BATC	Bulk Average Thermal Conductivity
BATKE	Bulk Average Turbulent Kinetic Energy
BAV	Bulk Average Velocity
Pres.	Pressure
No.	Number
CHT	Coefficient of Heat Transfer
TI	Turbulence Intensity

ABSTRACT

In the present work, STAR-CCM+ CFD code was used to investigate steady state thermal hydraulic parameters in the core of Ghana Research Reactor-1 (GHARR-1). The core was segmented into 21 axial segments. 3D-CAD parametric solid modeler embedded in STAR-CCM+ was used to model the geometry. The geometry was discretized by the use of appropriate meshing models. GHARR-1 operating conditions were set as boundary conditions for the STAR-CCM+ simulation conducted. Heat flux specific to individual axial segment computed based on segment power peaking factors and surface area was applied at the wall of the flow channel. For each power level, mass flow rate and temperature were imposed as boundary conditions at the inlet. Standard k-ε turbulence model was adopted for the solution of the transported variables namely turbulent kinetic energy and its dissipation rate. The results obtained were validated with experimental data from GHARR-1 operation and observed to be in appreciable agreement. The plots of the evaluated flow parameters show that the heat applied at the surface of the flow channel is efficiently transferred to the bulk of the fluid. In addition, effective distribution of temperature in the domain was observed. With effective heat transfer coupled with uniform heat distribution, it could be stated that cooling of GHARR-1 fuel which is needed for safety operation of the facility is assured.

CHAPTER 1

INTRODUCTION

This chapter presents the problem statement and provides justification for the research. It also gives a background for the present study and the scope of work.

1. BACKGROUND

For a normal operation of a nuclear reactor, all the heat released in the system must be removed very effectively by the coolant. In a nuclear reactor system, liquid or gaseous coolant pass through the core and through other regions where heat is generated. The effectiveness of the coolant system is one of the most important considerations in safe operation and design considerations. For an efficient natural cooling process, it is necessary to fully understand the mechanism of heat dissipation under different operating conditions [1].

In the present study, the type of system considered is a single phase flow system as present in GHARR-1. The cooling process in GHARR-1 is by natural convection.

1.1 DESCRIPTION OF GHANA RESEARCH REACTOR-1 (GHARR-1)

GHARR-1 is a tank-in-pool type, low power research reactor, which is under-moderated with 10 irradiation sites (5 inside and 5 outside the beryllium annulus reflector) [2, 3]. GHARR-1 uses 90.2 % enriched U-Al alloy as fuel. The diameter of the fuel meat is 4.3 mm and the thickness of the aluminum cladding material is 0.6 mm. The total length of the element is 248 mm and the active length is 230 mm. The percentage of U in the UAl_4 dispersed in Al is 27.5 % and the loading of U-235 in the core with 344 fuel element is 990.72 g [4]

The reactor is designed to be compact and safe. It is used mainly for neutron activation analysis, production of short-lived radioisotopes and for education and training. The maximum thermal neutron flux at its inner irradiation site is $1\times10^{12}\ n.cm^{-2}.s^{-1}$. It is cooled and moderated with light water, and light water and beryllium act as reflectors. The fuel cage consists of 344 fuel pins, 4 tie and 6 dummy rods, a central control rod guide tube, upper and lower grid plates as presented in Figure 1.1.

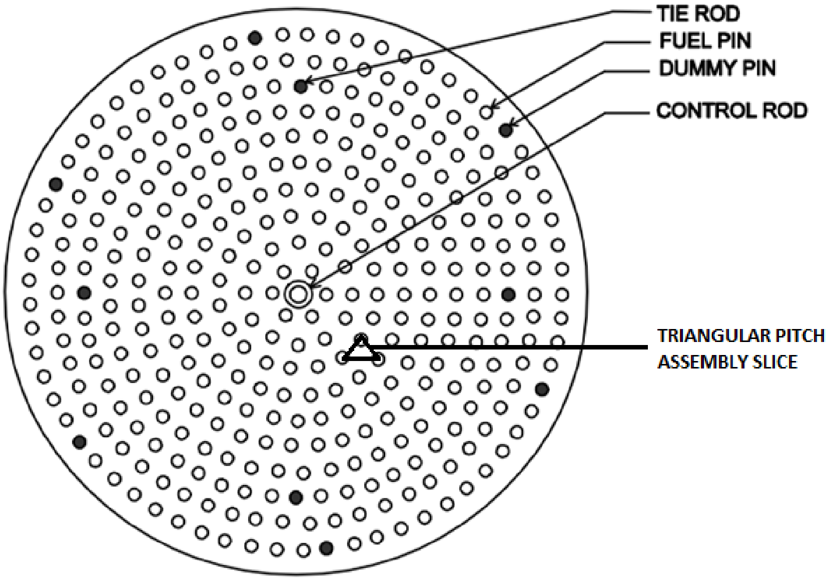

Figure 1.1: GHARR-1 fuel cage showing 344 fuel pins, 4 tie rods, 6 dummy rods and control rod

The fuel pins, tie and dummy rods are concentrically arranged in 10 rings of the fuel cage. The core has a central guide tube through which a cadmium control rod cladded in stainless steel moves to cover the active length of 230 mm of the core. The single control rod is used for regulation of power, compensation of reactivity and for reactor shutdown during normal and abnormal operations. The fuel cage is placed on a 50 mm thick beryllium reflector of diameter 290 mm and it is surrounded by another 100 mm thick metallic beryllium reflector of height 238.5 mm [4, 5, and 6].

The core is cooled by natural convection and under normal operating conditions, the flow regime is single phase but nucleate boiling is expected under abnormal condition when power excursion occurs due to large reactivity insertion. There are two pairs of NiCr-NiAl thermocouples, which are fixed in the inlet and outlet of the core coolant for measuring the temperature difference between the inlet and the outlet of the coolant. A platinum resistance thermometer is used for measuring the inlet temperature of the coolant [4, 5, and 6]. The coolant flow in the core is at the transient phase from laminar flow to turbulent flow. The flow transition will occur when there is an increase in power. The closer to the upper part of elements, the stronger the turbulence becomes [5]. A diagrammatic representation of the heat transfer mechanism is presented in Figure 1.2.

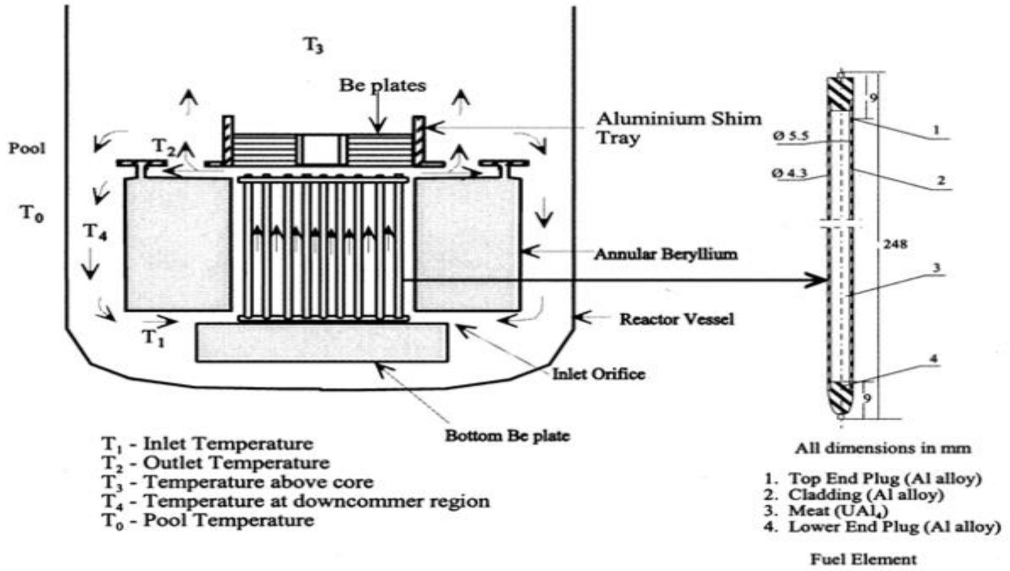

Figure 1.2: heat transfer mechanism in GHARR-1 [7]

Table 1.1 and Table 1.2 provides the technical and physical specifications for GHARR-1 respectively.

Table 1.1: Technical Specifications for GHARR-1

S/No	Geometries	Dimensions
1	Core Shape	Cylinder
2	Core height	23 cm
3	Core diameter	23 cm
4	Number of fuel elements	344
5	Fuel rod diameter (external)	5.5 mm
6	Fuel rod diameter (external)	4.3 mm
7	Number of dummy rods	6
8	Dummy rod diameter	5.5 mm
9	Number of tie rods	4
10	Tie rod diameter	5.5
11	Total lattice position	356
12	Number of control rods	1
13	Control rod diameter	5 mm
14	Guide tube thickness	3 mm
15	Guide tube diameter	6 mm
16	Number of Segmentation	21
17	Segment Length	10.95 mm

Table 1.2: Physics Specification for GHARR-1

S/No	Initial Conditions	Magnitude
1	Pressure at inlet	1 bar
2	Flow rate	400L/h (0.111 kg/s)
3	Density of water	999.7 kg/ m3
4	Initial temperature used	307.15 K
5	Power	15 KW
6	Velocity	0.002 m/s

1.1.1 Natural Convection

In GHARR-1, the water in the reactor core is not pressurized and it relies upon natural convection [8]. Natural Convection Processes are driven by body forces exerted directly within the fluid as a result of heating or cooling [9]. Natural convection is a mechanism, or type of heat transport, in which the fluid motion is not generated by any external source (like a pump, fan, suction device, etc.) but only by density differences in the fluid occurring due to temperature gradients. In natural convection, fluid surrounding a heat source receives heat, becomes less dense and rises. The surrounding, cooler fluid then moves to replace it. This cooler fluid is then heated and the process continues, forming a convection current; this process transfers heat energy from the bottom of the convection cell to top. The driving force for natural convection is buoyancy, a result of differences in fluid density [10].

Single phase flow is the flow of a material, as a gas, single-phase liquid, or a solid, but not in any combination of the three [11]. In GHARR-1 the flow regime is single phase deionized water.

1.1.2 GHARR-1 thermal hydraulic associated with heat removal

For safety analysis of MNSR's, a detailed understanding of the reactor heat transfer and distribution is necessary. The core region of GHARR-1 is located 4.7 m under water close to the bottom of a watertight reactor vessel. The quantity of water is 1.5 m^3 in the vessel, which serves the purpose of radiation shielding, moderation and as primary heat transfer medium. In addition, heat can be extracted from the water in the vessel by means of a water-cooling coil located near the top of the vessel. The water-filled reactor vessel is in turn immersed in a water-filled pool of 30 m^3. Cold water is drawn through the inlet orifice by natural convection. The water flows past the hot fuel elements and comes out through the core outlet orifice. The hot water rises to mix with the large volume of water in the reactor vessel and to the cooling coil. Heat passes through the walls of the container to the pool water. The reactor core is immersed in a large reactor vessel containing deionized water, which possesses a considerable heat capacity. Even under accident conditions, removal of heat is by natural circulation to this large heat sink. The core inlet flow orifice impedes the natural circulation of water through the core. Its area is fixed during assembly of the reactor and it is deliberately chosen such that the highest power achieved during the design basis self-limiting power excursion can cause no damage to the core or present any hazard to staff about the reactor. From thermal-hydraulic tests and calculations, especially from the transient experiment, it has been found that the reactor has negative feedback effect. Hence**,** when the temperature difference between the inlet and outlet coolant of the reactor increases, the buoyancy and circulating head will increase to make the flow velocity rise and in turn, limit the increase in power [8].

1.1.3 GHARR-1 Heat Transfer Distribution

One of the most important effects produced from fission reaction is the enormous amount of heat produced which must continually be removed in order to maintain the integrity of the reactor core components. A clear understanding of the thermal hydraulics associated with heat removal resulting from the nuclear fission is key to controlling and ensuring normal reactor operation. In GHARR-1 heat is produced in the nuclear fuel through fission reaction resulting from neutron bombardment of feasible isotope of uranium. The produced heat is conducted and removed by the coolant. For purposes of safety and design, the heat is circulated or transported via the coolant system to different locations in the reactor. For MNSR reactors which use natural convection for cooling, the generated heat is transferred in an upward direction from the base of the core. The heated water, which moves to the upper section of the reactor tank, is transferred to the pool water via conduction through the reactor vessel [7, 8]. The core is cooled by natural convection and under normal operational conditions, the flow regime is single phase but nucleate boiling is expected under abnormal condition when power excursion occurs due to large reactivity insertions. A platinum resistance thermometer is used for measuring the inlet temperature of the coolant [7].

1.2 PROBLEM STATEMENT

Reactor design and operation is limited by heat transfer consideration and not neutronic [12]. This is because the reactor core can withstand a neutron flux of any magnitude as long as the heat generated as a result of the fission reaction can be efficiently removed. It is on the basis of safety guided by thermal consideration that fuel, coolant and other structural materials are selected during design.

Previous research [7, 13] conducted on heat transfer for GHARR-1 were performed using 1-D codes namely PARET and PLTEMP thermal hydraulic codes. However, these 1-D codes do not provide detailed information on the variation of the trends of flow field parameters at specific locations within the core. The mass flow rate of the coolant at which effective heat transfer removal from the fuel is obtained is unknown. Also, previous studies offers no explanation on turbulent intensity of GHARR-1 core coolant.

1.4 JUSTIFICATION FOR RESEARCH

In GHARR-1 core, heat generated in the fuel is removed by natural convection. Ineffective heat transfer in the reactor core will lead to degradation of the fuel element, reactor vessel, or both. The knowledge of heat transfer and distribution in GHARR-1 will help inform its safe operation and optimization of the heat transfer processes.

Previous research on GHARR-1 -core heat transfer were done with 1-D generated codes and results obtained provided limited information. However with the application of the STAR-CCM+ it is deemed that improved analysis will be conducted to produce more reliable and detailed results. In addition STAR-CCM+ has the advantage of 3-D visualization and hence offer improved appreciation of the results.

1.4 RESEARCH OBJECTIVES

The present research aims to analyze heat transfer and distribution in the core of GHARR-1 using STAR-CCM+ code at different power levels. The specific objectives to be attained are,

1. To model a simplified GHARR-1 core that mimics the thermal hydraulics of the full GHARR-1 geometry using 3-D CAD model available in STAR-CCM+.
2. To generate a suitable mesh for the modelled geometry. Using the STAR-CCM+ Code.
3. To select appropriate physics models for the case under study
4. Perform simulation at various reactor power level at a step increase of 5 kW for 5-30 kW.
5. Analyse the generated data for steady state thermal-hydraulic performance of GHARR-1.

1.5 SCOPE OF RESEARCH

In the present work, STAR-CCM+ Code is used to analyze thermal hydraulic parameters of a simplified GHARR-1 core for the range 5-30 kW power levels. The work is limited to a steady state single phase flow without kinetics considerations.

This research is reported in five chapters. The next section discusses the outline of write-up presentation.

1.6 ORGANIZATION OF THESIS

Chapter 2 discusses general review of literature on heat transfer for research reactors with emphasis on low power research reactors of the MNSR type. And it also provides a review of the Reynolds Average Navier Stoke's (RANS) turbulence model used in STAR-CCM+ code. In Chapter 3, the method of solution and experimental procedure are presented. Chapter 4 provides validation of the simulated results and discusses result of the research findings. Chapter 5 is the concluding chapter where conclusions and deductions are made for each of the results discussed in chapter 4. This chapter also presents suggestion for possible areas of further studies.

In this chapter the research problem has been stated and justified and a background of the study provided. The next chapter presents review of related literature for the current study. It also provides some review on the capabilities of STAR-CCM+ used for the simulation.

CHAPTER 2

LITERATURE REVIEW

The present chapter presents review of related literature for the present study. It also provides some review on the capabilities of STAR-CCM+ CFD code used for the simulation.

2.1 INTRODUCTION

Interest in safety issues of nuclear research reactors is increasing due to increased application of neutrons for several types of scientific and social purposes in addition to power generation. To ensure safe utilization of such installations several codes have been used with special attention to research reactors. A combination of codes for thermal hydraulic analysis, for assessment of probabilistic risk, fuel investigation and reactor physics studies are fundamental tools for an appropriate reactor behavior definition [14]. Research reactor types include Siemens Unterrichtsreaktor, Argonaut reactor, Slowpoke reactor, the miniature neutron source reactor, TRIGA reactors, Material testing reactors and High flux reactors [15]. One of such codes used in nuclear industries is the STAR-CCM$^+$ CFD code which is employed for the present study. The features of this code are presented in section 2.2.

2.2 COMPUTATIONAL FLUID DYNAMIC (CFD) TOOL

CFD codes comprise of pre-processor, solver and post-processor phases. The preprocessing is concerned with the geometry modelling, definition of material properties, mesh generation and physics definition [16]. The CFD codes solver section deals with the solver type specification and analysis runs. It solves the transport equations on every node defined during the mesh generation step and any additional models specified in the physics set up [17]. For post processing, CFD codes allow for setting different plots and scenes either before, during or after running the simulation. These plots and scenes are then analyzed on attainment of convergence of the solution.

For the present work, STAR-CCM+ CFD code is considered for investigation of heat transfer and distribution. STAR-CCM$^+$ is a comprehensive engineering simulation tool used to solve problems involving fluid flow, heat transfer, condensation and stability analysis just to mention a few [18]. STAR-CCM+ is a CFD code structured around numerical algorithms that can tackle fluid flow problems accounting for turbulence effects [19, 20] as it employs the Finite Volume Approach to address a wide variety of modeling needs. STAR-CCM+ is equipped with the following;

- 3D-CAD modeler
- Surface preparation tools
- Automatic meshing technology
- Physics modeling options
- Turbulence modeling options
- Post-processing and monitors

The object-oriented nature of STAR-CCM+ code can be seen in the user interface presented in Figure 2.1.

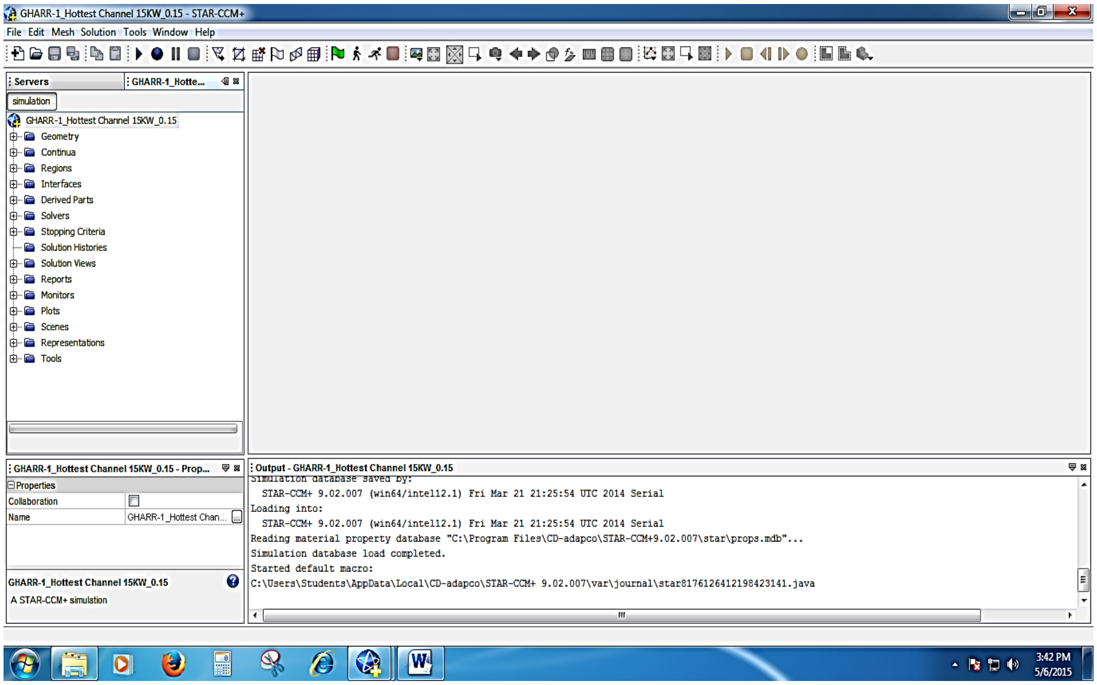

Properties

Collaboration ☐

Name GHARR-1_Hottest Chan...

GHARR-1_Hottest Channel 15KW_0.15

A STAR-CCM+ simulation

```
Simulation database saved by:
  STAR-CCM+ 9.02.007 (win64/intel12.1) Fri Mar 21 21:25:54 UTC 2014 Serial
Loading into:
  STAR-CCM+ 9.02.007 (win64/intel12.1) Fri Mar 21 21:25:54 UTC 2014 Serial
Reading material property database "C:\Program Files\CD-adapco\STAR-CCM+9.02.007\star\props.mdb"...
Simulation database load completed.
Started default macro:
C:\Users\Students\AppData\Local\CD-adapco\STAR-CCM+ 9.02.007\var\journal\star8176126412198423141.java
```

Figure 2.1: STAR-CCM+ user Interface

Geometry window allows for modeling of studied dimensions using the 3D-CAD within STAR-CCM+. This also allows for exporting geometry from 3D-CAD and ascending the modelled geometry in the simulation. Continua window is concerned with physics and the mesh continuum. This allows the user to input the properties of materials and also give the properties of the mesh. It also allow users to specify boundary conditions to be imposed on various parts. Solvers window works with chosen meshing and physics models to attain solutions and communicate them to the user. The user-specified models provide the required transport equations to be solved by the solver. Derived parts window allow user to set up probes and constraint planes at any point within or outside the geometry. The available windows are used to specify model properties by utilizing the STAR-CCM+ models described in section 2.2.1.

2.2.1 STAR-CCM+ Models

2.2.1.1 Physics Models

The governing equations used for command execution by STAR-CCM+ solver are the conservation of mass, momentum and the energy equations given in equations 2.1 to 2.5.

2.2.1.2 Continuity Equation

$$\frac{\partial \rho}{\partial t} + \frac{\partial(\rho u)}{\partial x} + \frac{\partial(\rho v)}{\partial y} + \frac{\partial(\rho w)}{\partial z} = 0 \qquad (2.1)$$

where ρ is the density, t is time (s), x, y and z are components of momentum in x, y and z planes respectively, u, v and w are components of velocity corresponding to x, y and z planes respectively.

2.2.1.3 Momentum Equations

U- Momentum

$$\frac{\partial(\rho U)}{\partial t} + \frac{\partial}{\partial x}\left(\rho U^2 - \mu e\frac{\partial U}{\partial x}\right) + \frac{\partial}{\partial y}\left(\rho UV - \mu e\frac{\partial U}{\partial y}\right) + \frac{\partial}{\partial z}\left(\rho UW - \mu e\frac{\partial U}{\partial z}\right) = -\frac{\partial p}{\partial x} + \rho g_x \qquad (2.2)$$

V- Momentum

$$\frac{\partial(\rho U)}{\partial t} + \frac{\partial}{\partial x}\left(\rho UV - \mu e\frac{\partial U}{\partial x}\right) + \frac{\partial}{\partial y}\left(\rho V^2 - \mu e\frac{\partial U}{\partial y}\right) + \frac{\partial}{\partial z}\left(\rho VW - \mu e\frac{\partial V}{\partial z}\right) = -\frac{\partial p}{\partial y} + \rho g_y \qquad (2.3)$$

W-Momentum

$$\frac{\partial(\rho W)}{\partial t} + \frac{\partial}{\partial x}\left(\rho UW - \mu e\frac{\partial W}{\partial x}\right) + \frac{\partial}{\partial y}\left(\rho VW - \mu e\frac{\partial W}{\partial y}\right) + \frac{\partial}{\partial z}\left(\rho W^2 - \mu e\frac{\partial W}{\partial z}\right) = -\frac{\partial p}{\partial z} + \rho g_z \qquad (2.4)$$

where, ρ is the density of the fluid, P is the pressure, and τ is the viscous stress

2.2.1.4 Energy Equation

$$\rho\frac{DE}{Dt} = -div(pu) + \left[\frac{\partial(u\tau_{xx}}{\partial x} + \frac{\partial(u\tau_{yx})}{\partial y} + \frac{\partial(u\tau_{zx})}{\partial z} + \frac{\partial(v\tau_{xy})}{\partial x} + \frac{\partial(v\tau_{yy})}{\partial y} + \frac{\partial(v\tau_{zy})}{\partial z} + \frac{\partial(w\tau_{xz})}{\partial x} + \frac{\partial(w\tau_{yz})}{\partial y} + \frac{\partial(w\tau_{zz})}{\partial z} + div(kgradT) + S_E\right] \tag{2.5}$$

2.2.1.5 K-Epsilon Turbulence Models

A k-Epsilon turbulence model is a two-equation model in which transport equations are solved for the turbulent kinetic energy and its dissipation rate [15].

$$\frac{d}{dt}\int_V \rho k dV + \int_A \rho k\left(v - v_g\right).da = \int_A \left(\mu + \frac{\mu_t}{\sigma_k}\right)\nabla k.da + \int_V \left[G_k + G_b - \rho\left((\varepsilon - \varepsilon_o) + \Upsilon_m\right) + S_k\right]dV \tag{2.6}$$

$$\frac{d}{dt}\int_V \rho\varepsilon dV + \int_A \rho\varepsilon\left(v - v_g\right).da = \int_A (\mu + \frac{\mu_t}{\sigma_\varepsilon})\nabla\varepsilon.da + \int_V \frac{1}{T}\left[C_{\varepsilon 1}(G_k + G_{nl} + C_{\varepsilon 3}G_b) - C_{\varepsilon 2}\rho\left((\varepsilon - \varepsilon_o) + \rho\Upsilon_y\right) + S_\varepsilon\right]dV \tag{2.7}$$

where S_k and S_ε are the user-specified source terms. ε_o is the ambience turbulence value in source terms that counteract turbulence decay[21 , 16]

The turbulence production rate G_k is evaluated as:

$$G_k = \mu_t S^2 - \frac{2}{3}\rho k\nabla.V - \frac{2}{3}\rho(\mu_t\nabla.V)^2 \tag{2.8}$$

The production due to buoyancy G_b is evaluated as:

$$G_b = \beta\frac{\mu_t}{\sigma_t}(\nabla T.g) \tag{2.9}$$

where β is the coefficient of thermal expansion is, g is the gravitational vector, ∇T is the temperature gradient vector and σ_t is the turbulent Prandtl number.

.By default $C_{\varepsilon 3}$ it is computed as [22, 16]:

$$C_{\varepsilon 3} = tanh\frac{|v_b|}{|u_b|} \qquad (2.10)$$

Where v_b the velocity vector component is parallel to g, and u_b is the velocity vector component perpendicular to g.

For compressibility modification, the dilation dissipation Υ_m is modelled according to Sarkar as:

$$\Upsilon_m = \frac{C_M k_\varepsilon}{c^2} \qquad (2.11)$$

Where c is the speed of sound and $C_M = 2$

The turbulent viscosity is computed as:

$$\mu_t = \rho C_\mu kT \qquad (2.12)$$

The model coeficients are presnted tin equation 2.9.

$$C_{\varepsilon 1} = 1.44, \quad C_{\varepsilon 2} = 1.92, \quad C_\mu\ 0.09, \quad \sigma_k = 1.0,$$
$$\sigma_\varepsilon = 1.3, \quad C_t = 1 \qquad (2.13)[16]$$

The turbulence models are executed using the specified meshing and physics models. The meshing and physics models are described in section 2.2.2 and 2.2.3.

2.2.1.6 Wall Y+

In STAR-CCM+, each turbulence model has a set of near-wall modeling assumptions known as wall treatment. Three wall treatment types exist namely; all y+, low y+ and high y+. The all y+ wall treatment is a hybrid treatment that emulates the high y+ wall treatment for coarse meshes and the low y+ wall treatment for fine meshes [16]. The meshing model are selected to suit the intended physics models to be employed for the solution. The physics models are described in section 2.2.3.

2.2.1.7 Segregated Flow Model

Segregated flow model was applied to the studied liquid material model to solve the flow equations (one for each component of velocity, and one for pressure) in an uncoupled manner. The linkage between the momentum and continuity equations is achieved with a predictor-corrector approach [16].

2.2.1.8 Three-Dimensional Model

The Three-Dimensional model is designed to work on three-dimensional meshes [16], and is activated for the three-dimensional mesh chosen for the present work. In addition to the use of thermal CFD codes, there exist other methods of thermal hydraulics studies. Previous research done in this aspect are reviewed in section 2.3.

2.3 THERMAL HYDRAULIC STUDIES

Thermal Hydraulic Behavior of Research Reactor during Natural Convection Cooling Mode was studied Talha [1] using experimental apparatus designed and constructed to simulate the cooling process through the channel in the core of research reactor during natural cooling. The measurements included the effect of the pool temperature, heat flux and the height of the chimney (extension ratio), on the coolant velocity, heat transfer coefficient, coolant temperature and surface temperature. The cooling channel was made from two heated vertical parallel plates of aluminum alloy acting as a vertical rectangular channel where water was used as a cooling fluid. Experiment was carried out under the atmospheric conditions. The measurements were done for free convection from vertical iso-flux and parallel walled channels to explore the heat transfer enhancement due to adding the adiabatic extensions of different heights (15, 35 and 55 cm) to the heated channel. The coolant velocity and the heat transfer coefficient increased with increase in the heat flux at constant coolant inlet temperature. For constant heat flux the coolant velocity increased and the heat transfer coefficient is enhanced by the increase of the coolant inlet temperature [1]. The present work considers the effect of coolant inlet temperature on heat transfer and distribution at different positions of a flow channel for a natural convection cooling process.

In a previous work performed by Annafi [2**],** development of a mathematical model to study the transient heat distribution within Ghana Research Reactor -1 (GHARR-1) fuel element and related shutdown heat generation rates. The shutdown heats considered were residual fission and fission product decay heat. A finite difference scheme for the discretization by implicit method was used. Solution algorithms were developed and MATLAB program implemented to determine the temperature distributions within the fuel element after shutdown due to reactivity insertion accident. The simulations showed a steady state temperature of about 341.3 K which deviated from that reported in the GHARR-1 Safety Analysis report by 2 % error margin. The average temperature obtained under transient condition was found to be approximately 444 K which was lower than the melting point of 913 K for the Aluminum cladding. The present work however will not employ MATLAB but rather use a more sophisticated CFD tool to address similar issues that were the focus in the work of Annafi [2]. But by contrast the present work utilizes heat flux imposed at the wall surface for steady state heat transfer and distribution analysis under normal operation of GHARR-1.

Another research performed by Okon [23] employed an analytical approach of the general heat conduction differential equation in cylindrical coordinate to solve the temperature distribution and heat flux for the nuclear fuel element. They were able to show the transient temperature behavior by solving analytically the heat transfer equation using Green's functions and also developed from first principle the transient temperature equations for the fuel element. Results obtained showed that, the transient temperature distribution decreased from the center of the fuel to the surface of the cladding and followed a parabolic decay pattern after increase in time. As in the described Okon [23], the present work will also seek to study the heat distribution from the surface of a cylindrical fuel clad into the coolant at varying reactor powers. Similarly, in the present work a cylindrical core is considered for analyzing temperature distribution but in the core coolant of GHARR-1.

A previous work performed by Ganesh [24] determined the velocity profile of coolant flow in the Ghana Research Reactor-1 (GHARR-1). Finite difference scheme for the discretization by Marker and Cell (MAC) method was used in the model. Solution algorithms were developed and MATLAB program implemented to simulate the velocity distribution of coolant flow at a 30 kW nominal power. The fluid dynamics module of the Navier-Stokes Equations (NSEs) in COMSOL Multiphysics v 3.4 was used to verify and validate the results obtained. The results showed a velocity distributions range of 0.9 m/s to 1.9 m/s. Reynolds number values ranging from 460 to 970 were also obtained indicating a laminar flow of coolant. The present work considers the analysis of turbulent intensity determined from the coolant mean velocity and turbulent kinetic energy.

The fluid dynamics module of the NSEs in COMSOL Multiphysics was used to validate the results. The models considered for the present work utilizes Navier-Stokes equation for energy, continuity and momentum for the simulation which will be validated with experimental data.

Analysis of flow stability in nuclear reactor sub-channels with water at supercritical pressures presented results of analysis by CFD models of flow stability in fuel bundle slices with upward, horizontal and downward flow orientations had been reported by Ampomah-Amoako [7]. Square and triangular lattice slices were both studied, basing on previous work that demonstrated the feasibility of such analyses. A non-uniform heat flux is applied to the slice walls without addressing the internal structure of the rod. The present work will not consider the coolant subchannel but the cylindrical flow channel. The present work however considers the application STAR-CCM+ code on the more general circular flow channel for GHARR-1 with a non-uniform heat flux imposed on the wall surface. Thermal hydraulic studies are done to determine heat transfer parameters of interest. Section 2.4 discusses heat transfer and distribution parameters.

2.4 HEAT TRANSFER AND PARAMETERS

Heat flux density is the heat rate per unit area. In SI units, heat flux density is measured in [W/m^2] [26]. Heat flux is quantified mathematically by equation 2.14.

$$\Phi = \frac{P}{A} \tag{2.14}$$

Where Φ is the heat flux, P is power and A is the area.

The heat transfer coefficient is proportionality coefficient between the heat flux and the thermodynamic driving force for the flow of heat (i.e., the temperature difference, ΔT). The coefficient of heat transfer is described by equations 2.15 and 2.16.

$$h = \frac{q}{A\Delta T} \tag{2.15}$$

$$\Delta T = T_s - T_b \tag{2.16}$$

where: A is area, q is power, T_s is surface temperature T_b is bulk Temperature

Turbulence or turbulent flow is a flow regime characterized by chaotic property changes. This includes low momentum diffusion, high momentum convection, and rapid variation of pressure and flow velocity in space and time. Turbulence kinetic energy (TKE) is the mean kinetic energy per unit mass associated with eddies in turbulent flow. Physically, the turbulence kinetic energy is characterized by measured root-mean-square (RMS) velocity fluctuations. Turbulence is concerned with fluctuations in fluid flow. A steady fluid flow would have low turbulence. An unsteady fluid flow would have higher turbulence. Turbulence Intensity is that measurement scale for expressing the degree of turbulence. It is given by equation 2.15 and 2.16.

$$I = \frac{\acute{\upsilon}}{\tilde{v}} \tag{2.15}$$

where $\tilde{v}$ is the mean flow fluid bulk average velocity and

$$\acute{\upsilon} = \sqrt{\frac{2}{3}k} \tag{2.16}$$

where k is the fluid bulk turbulence kinetic energy

From the above review, it is established that there is need for thermal hydraulic studies using a code that has the ability to precisely analyze a wide range of thermal hydraulic parameters. Details of methodology employed for studying the heat transfer parameters using STAR-CCM+ is presented in the next chapter.

CHAPTER 3

METHODOLOGY

This chapter presents the methodology adopted to achieve the objective specified in section 1.4 of chapter 1. This include detailed procedure of experimentation performed to obtain data for validation of the simulation work.

3.1 Experimental

The experimental data to be used for validation of simulation results were obtained using the Ghana Research Reactor-1 at Ghana Atomic Energy Commission Research Reactor facility Centre. The experiment was conducted for normal operating conditions at different power levels (5 kW to 30kW at interval of 5 kW). Six readings were taken at an average of 30 minutes interval for each power level and the inlet and outlet temperatures were noted.

For 15 kW power, the flux monitor recorded a constant flux of 4.68×10^{11} n/cm^{2}s even as the control rod position varied between a minimum of 129 mm to a maximum of 143 mm at inconsistent interval of 1-5 mm. The mean inlet and outlet temperatures were found to be 313.42 K and 323.59 K respectively. For 20 kW power, Inlet and outlet temperatures were obtained using a pre-set neutron flux of 6.67×10^{11} n/cm^{2}s. The control rod position was varied from a minimum of 152 mm to a maximum of 169 mm to obtain five inlet and outlet temperatures at an interval of 10 minutes. The mean inlet and outlet temperatures were found to be 316.65 K and 327.91 K respectively. Reactor power of 25 kW was obtained at a pre-set neutron flux of 8.33×10^{11} n/cm^{2}s with control rod position varied from a minimum of 160 mm to a maximum of 182 mm. Mean inlet and outlet temperatures obtained are 314.39K and 328.25 K respectively.

Reactor power of 30 kW was attained at a pre-set flux of 1.0×10^{12} n/cm^{2}s was used to obtain seven set of inlet and outlet temperatures with a minimum and maximum control rod position of 165 mm to 185 mm at an interval of between 2 mm and 5 mm. The mean inlet and outlet temperatures were 316.32 k and 331.26 K respectively.

For lower powers (5kW and 10 kW), a flux less than 4.68×10^{11} n/cm^{2}s and control rod position greater than 129 mm was used with inlet and outlet temperature of 38.5 and 38.75 for 5 kW power and 42.85 and 46.5 for 10 kW power respectively. The inlet and outlet temperatures were measured using the two pairs of NiCr-NiAl thermocouples, which are fixed in the inlet and outlet of the reactor core for measuring the temperature difference placed at T_1 and T_2 in figure 1.2.

The power released in a reactor is related to flux by equation 3.1

$$P = \frac{\Phi_{th}\Sigma_f V}{3.12\times10^{10}\,\frac{fissions}{watt-sec}} \qquad (3.1)$$

where:

P = power (watts)

Φ_{th} = thermal neutron flux (neutrons/cm^2 -sec)

Σ_f = macroscopic cross section for fission (cm^{-1})

V = volume of core (cm^3)

3.2 STAR-CCM+ SIMULATION

3.2.1 Geometry Modeling

The geometry adopted for the flow channel is coherent with the core configuration of GHARR-1 and is obtained as shown in Figure 3.1. Modifications were made on the geometry previously used [7] by using 3D CAD model available in the STAR-CCM$^+$ CFD code. The modification however did not include the radius of the geometry. The reduction in the length by a factor of 10 gives rise to a geometry of total length 0.023 cm. The geometry modification was based on the availability of limited computational memory. The resulting length was further sectioned into 21 segments. Figure 3.1 shows the resulting geometry adopted for the present work.

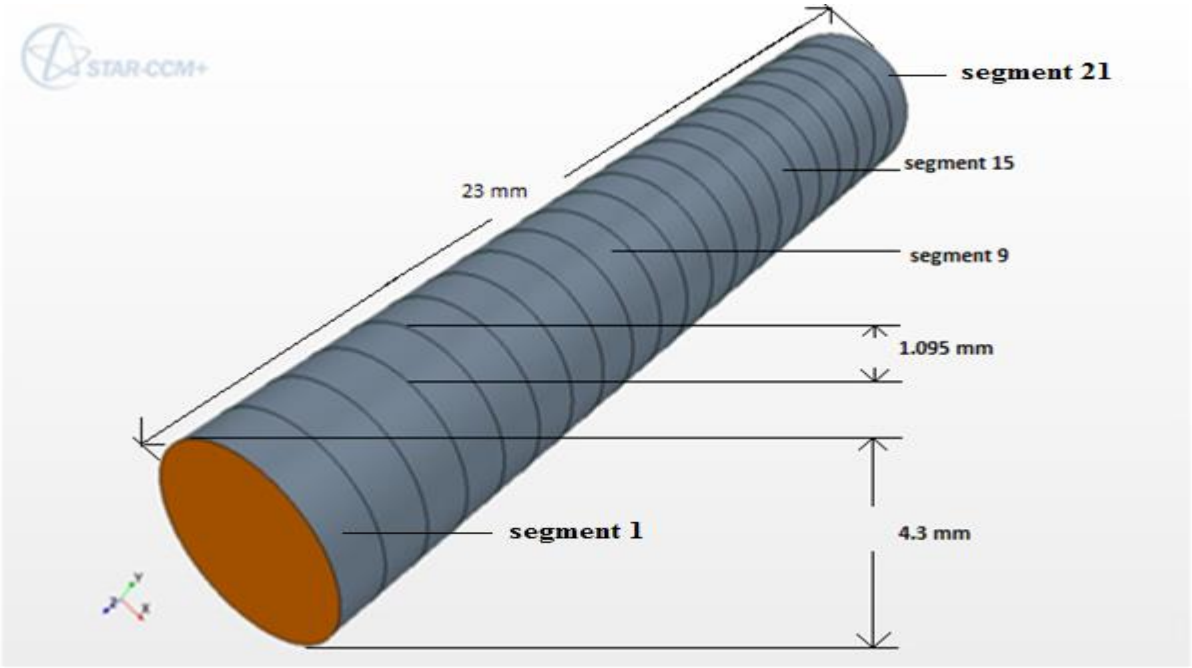

Figure 3.1: GHARR-1 core coolant modified geometry

3.2.2 Mesh Generation

The mesh generation pipeline consisted of surface remesher, polyhedral mesher and prism layer mesher. The surface remesher is chosen to re-triangulate the existing surface in order to improve the overall quality of the surface and optimize it for the volume mesh models. The polyhedral meshing model was utilized with the prism layer mesh in order to generate orthogonal prismatic cells next to the wall boundaries. This layer of cells is necessary to improve the accuracy of the flow solution. The choice of the polyhedral mesh is to take advantage of its short turnaround time in building the mesh with solution accuracy and convergence rate. The properties of the meshing models adopted are shown in Table 3.1.

Table 3.1: Meshing Models

S/No	Mesh Models	Specification
1	Base Size	0.12mm
2	Prism Layer Stretching	1.11
3	Prism Layer Thickness	0.5 mm
4	Number of Mesh cells	553928
5	Surface growth rate	1.3
6	Number of Prism Layers	20

The resulting mesh generated after applying the above mesh models for the modified geometry is presented in Figure 3.2.

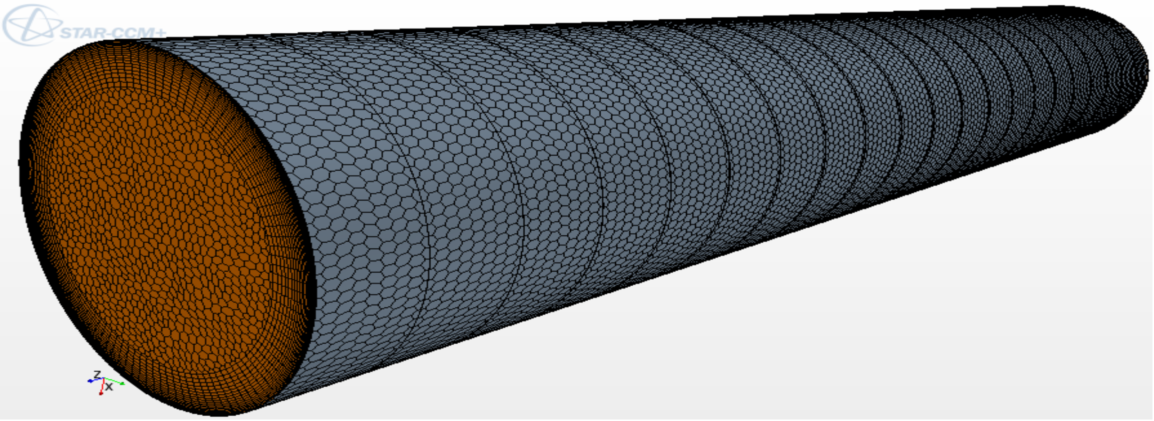

Figure 3.2: Mesh scene

3.2.3 Setting-up Physics

Physics models and boundary conditions employed for the present work are shown in table 3.2 below.

Table 3.2: Physics Model

S/No	Physics Model	Specification
1	Space Model	Three Dimensional
2	Time Model	Steady State
3	Material Model	Water
4	Flow Model	Segregated Flow
5	Energy Model	Segregated Fluid Isothermal
6	Viscous Regime Model	Turbulent
7	Turbulent Model	K-Epsilon
8	K-E Model	Standard K-E Turbulence
9	Wall Function	All Y+ Wall Treatment
10	Convection Scheme	2nd Order
	Boundary Condition	Specification
11	Inlet	Mass Flow Inlet inlet Temperature
13	Interface	Free Stream
14	Outlet	Pressure outlet
15	wall Surface	heat Flux

Segregated Flow model which is a suitable flow model for liquid material model was chosen in order to solve the required flow equations in an uncoupled manner. The linkage between the momentum and continuity equations is achieved with a predictor-corrector approach. This model has its roots in constant-density flows adequate for the steady state system presently studied. It is capable of handling mildly compressible flows and low Raleigh number natural convection. Unlike coupled flow which needs more resources like memory and computational time as it solves coupled equations for pressure and velocities.

The segregated flow model choice for the present study was due to memory availability limitation. The model is suitable for the studied material model whose density. The segregated fluid isothermal model was applied as the energy model to provide constant temperature field for all models that required temperature. In order to work with the three dimensional mesh, a three-Dimensional model was selected. The Steady model is selected because the system under study is a steady state system. When this model is activated, the concept of a physical time-step is meaningless. Second order Convection scheme was chosen for accuracy and stability of the solution. The all y+ wall treatment was selected because it is a hybrid treatment that attempts to emulate the high y+ wall treatment for coarse meshes and the low y+ wall treatment for fine meshes.

Thermometric input parameters (temperature, density, viscosity, and thermal conductivity) needed as boundary conditions were computed using the NIST online database. The computed thermometric properties are presented in Appendix A. The parameters were imposed at both the inlet and outlet and also on the surface boundaries. Figure 3.3 shows the boundary conditions adopted for the STAR-CCM+ simulation.

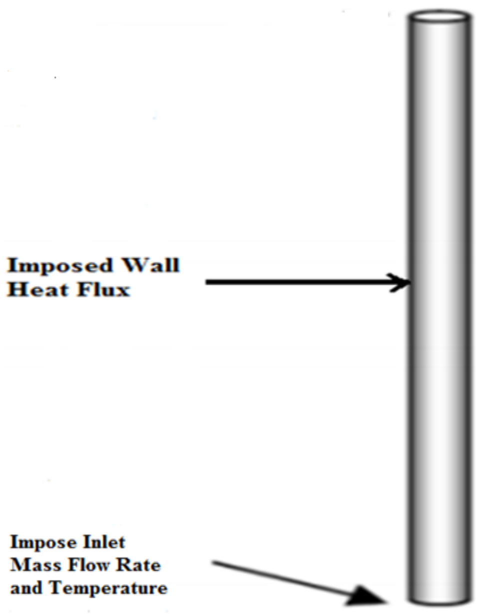

Figure 3.3: cylindrical flow channel showing imposed boundary conditions

For each power level mass flow rate and temperature were imposed as boundary conditions at the inlet. On the wall surface, a varying heat flux was imposed. The varying heat flux takes into consideration the power peaking factor for each segment. Pressure was imposed at the outlet.

Standard k-ε turbulence model available in the STAR-CCM+ code was adopted for the present study. The k-ε turbulence model is a two-equation model in which the equations for turbulent kinetic energy and its dissipation are solved. The modelled equations for k and ε and their coefficients are given in equations 2.6 and 2.7 respectively.

The governing equations of flow namely; continuity equation, energy equation and momentum equations given in equations 2.1 - 2.5 are solved over the domain. The solution were monitored to converge by assessing the residuals (Appendix F) and the trend of the outlet temperature. Figure 3.4 depicts contour plots of the fluid temperature development. After set-up, the simulation iterate for about 20 seconds before the onset of fluid development. Hence at 0-19 s given by Figure 3.4a the temperature scene is equal to the inlet temperature. Figure 3.4b shows the wall surface temperature distribution after 20 s. This temperature contour is influenced by the pattern of the imposed wall surface heat flux. Almost immediately, the temperature from the imposed heat flux is distributed marking the onset of temperature development within the fluid. In figure 3.4c after 3800 s the temperature can be seen building up from the inlet to the outlet. Fluid at higher temperature can be seen moving towards the outlet as presented in Figure 3.4d after 4500 s.

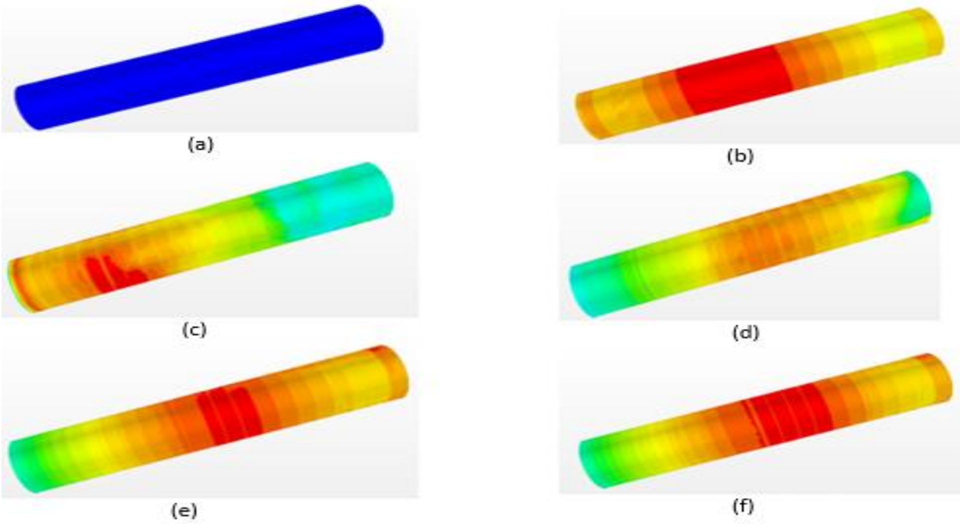

Figure 3.4: channel temperature development with time

It can be seen from Figure 3.4e and 3.4f that as the simulation progresses, the temperature distribution varies from inlet to outlet over time until it stabilizes after 5160 s when there is no significant difference in the temperature distribution on the wall surface. Figure 3.4f shows the temperature contour after 5400 s.

3.3 POWER PEAKING FACTORS CALCULATION

Computation of GHARR-1 power peaking factors was done by dividing each of the 344 fuel pins in the GHARR-1 core into 21 axial segments [7]. The temperature for each of these segments was calculated using MCNP neutronic code. The maximum temperature for each of the 21 axial segments was used to represent the temperature of the *hottest channel*. An average of the temperature for the 344 fuel pins was taken as the temperature of the *averaged channel*. The total calculated temperatures (344 × 21) were averaged to get the *core average* temperature. To calculate the power peaking factor, each of the 21 temperature values for hottest and averaged pins was divided over the core average. Table 3.3 gives the resulting power peaking factors for hottest and averaged channels.

Table 3.3: Power Peaking Factors for GHARR-1 Core [7].

Axial segment	Hottest Channel	Averaged channel
1	1.20363754	1.017745586
2	1.122930233	0.941616129
3	1.133713187	0.954228422
4	1.171182012	0.986920571
5	1.225387689	1.024269794
6	1.265911039	1.059170889
7	1.304844097	1.087226271
8	1.323840326	1.108510771
9	1.341304445	1.121339658
10	1.339559002	1.124731595
11	1.323064574	1.118235095
12	1.308936189	1.104893912
13	1.281755775	1.079923035
14	1.245305124	1.046968555
15	1.183962528	1.005700206
16	1.126624752	0.955673981
17	1.061025217	0.902197271
18	0.986058474	0.846280419
19	0.940349222	0.800489936
20	0.933006729	0.791342411
21	1.052918607	0.911237107

3.4 HEAT FLUX CALCULATION FOR THE MODIFIED GEOMETRY

The power peaking factors presented in Table 3.5 were used to calculate the imposed heat flux for each segment using equation 3.2. The computed heat fluxes are presented in Appendixes B and C.

$$\Phi_s = \frac{P_s}{A_s} \tag{3.2}$$

Where A_S is the surface area of the segment given by equation 3.3, Φ_s is the segment heat flux and P_s is the segment power given by equation 3.4

$$A = 2\pi \mathrm{rh} + 2\pi r^2 \tag{3.3}$$

Where r = segment radius, h = segment length. However, because of the geometry modification, the height was reduced from 10.95 mm to 1.095 mm.

$$P_S = \left(\frac{f_S}{f_T}\right) * P_R \tag{3.4}$$

Where P_s is the segment power, f_s is the segment power peaking factor, f_T is the total power peaking factor and P_R is the reactor power considered.

The resulting heat flux calculated for hottest and averaged channels are presented in appendix B and appendix C respectively.

Data obtained from the simulation was post-processed and plots were generated for analysis. The simulation generated results were validated with experimental data. In the next chapter, discussion of trends of plots generated from simulation data is presented.

CHAPTER 4

RESULTS AND DISCUSSION

4.1 INTRODUCTION

In this chapter details of results obtained from both experimental and simulation exercises are presented and discussed. Results of the simulation were obtained over constrained planes and line probes. Figure 4.1 shows the constrained planes. The constrained planes were placed at the inlet and outlet of each segment.

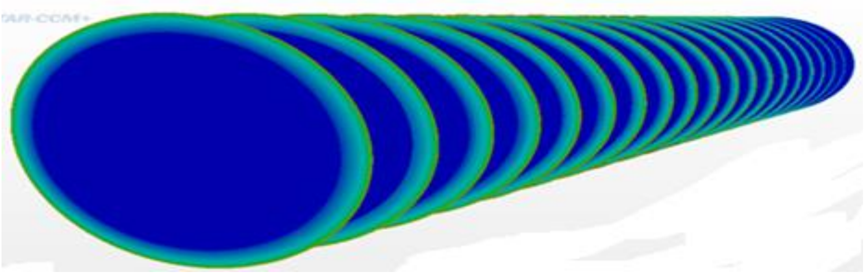

Figure 4.1: Position of constrained planes in the geometry

The solutions were also taken over line probes that are shown in figure 4.2. The line probes were placed at different points on the surface and within the fluid. Eight line probes were placed close to the wall and one at the center of the geometry. From the centerline probe, the next probe was placed at a distance of 2 mm and the subsequent line probes were placed at an increased distance of 0.02 mm interval.

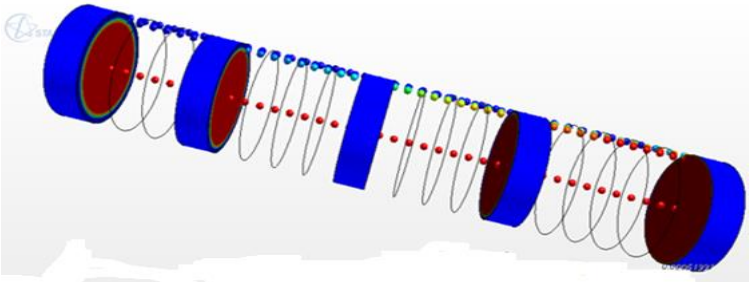

Figure 4.2: Position of line probes in the geometry

4.2 VALIDATION OF SIMULATION DATA

In order to determine the extent of prediction of the experimental data, plots of outlet temperature against power for the simulation were compared with data obtained experimentally. "Out Temp Exp", "Out Temp Sim Hot" and "Out Temp Sim Avr" used in the legend are abbreviations for experimental outlet temperature, simulation outlet temperature for hottest channel and simulation outlet temperature for averaged channel respectively. In the present work, hottest channel is the channel whose segment heat fluxes are calculated using the GHARR-1 power peaking factors for hottest channel presented in Table 3.6. Averaged channel is the channel whose segment heat fluxes were computed using the GHARR-1 power peaking factors for the averaged channel presented in Table 3.3.

Figures 4.3a and 4.3b shows plots of temperature against power for a uniform mass flow rate of 0.15 kg/s.

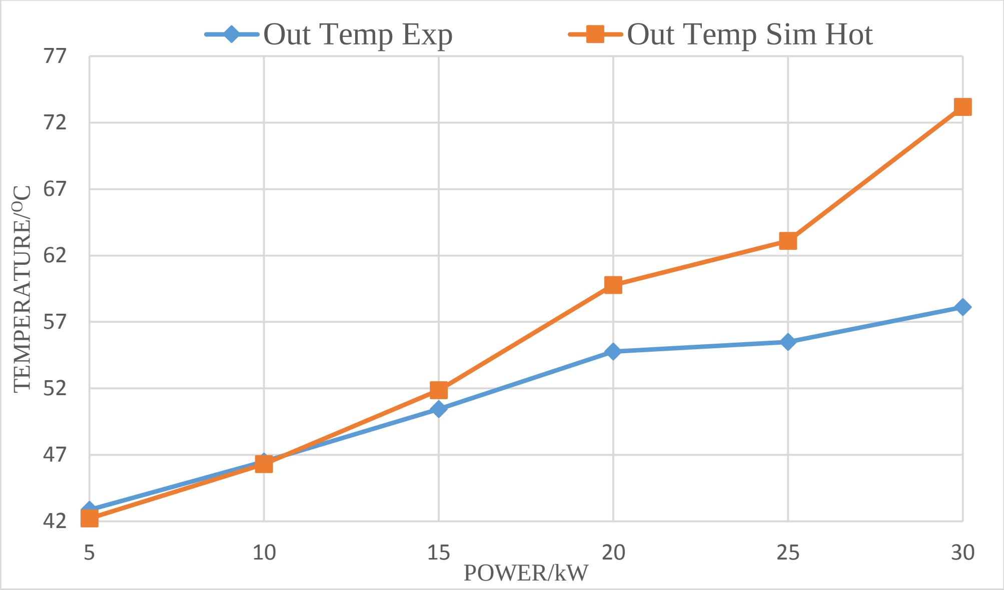

Figure 4.3a: Graph of outlet Temperature versus Power for hottest channel

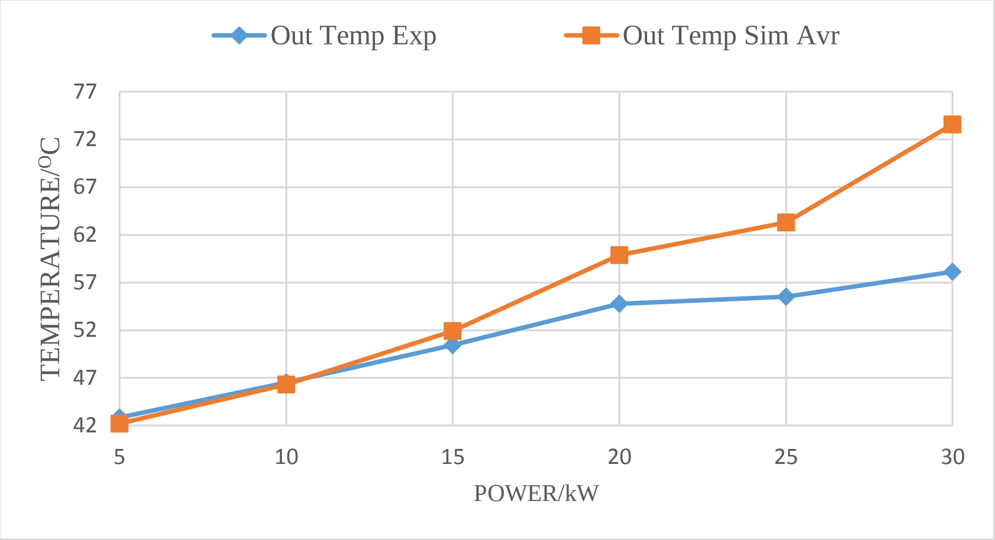

Figure 4.3b: Graph of outlet Temperature versus Power for averaged channel

In Figures 4.3a and 4.3b, a mass flow rate of 0.15 kg/s was used for simulation at 5 kW – 30 kW. This mass flow rate corresponds to the mass flow rate stated for normal operation of GHARR-1 [3]. The simulated result for 5kW to 15 kW agrees closely with the experimental result but between 15 kW and 30 kW, a marked deviation of the simulation data from the experimental was observed. The deviation observed could be due to inadequate cooling which led to ineffective removal of heat generated at 20 kW to 30kW.

The mass flow rate in the 30 kW power was increased in order to investigate the effect of increased coolant volume on the simulation outlet temperature. Figures 4.4a and 4.4b show plots of temperature against power obtained after varying the mass flow rate for the simulation at 30 kW from 0.15 kg/s to 0.2 kg/s.

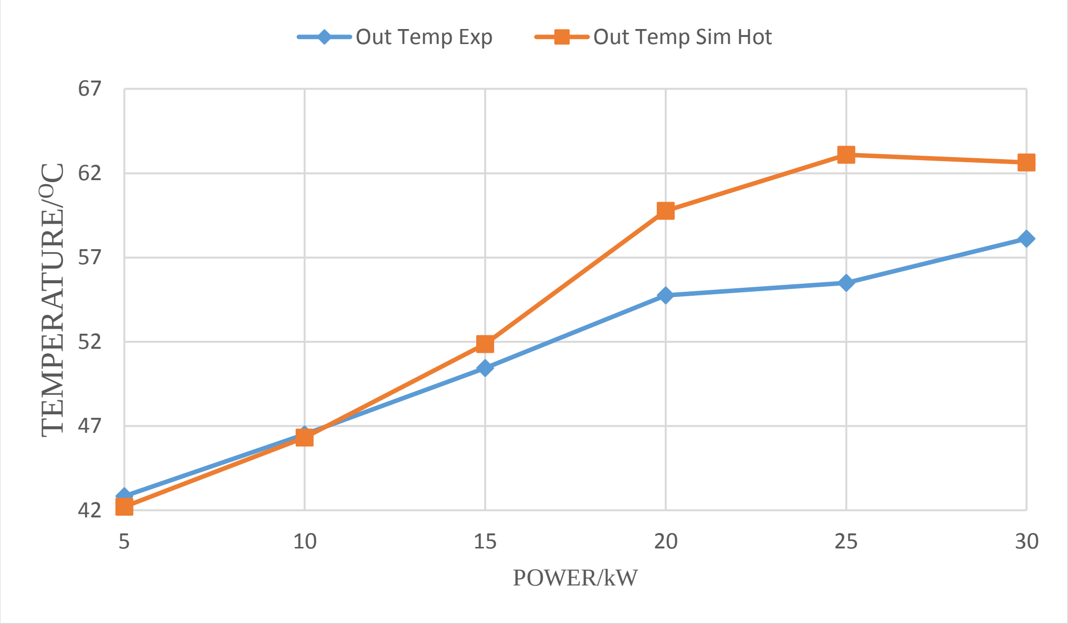

Figure 4.4 a: Graph of outlet Temperature versus Power for hottest channel

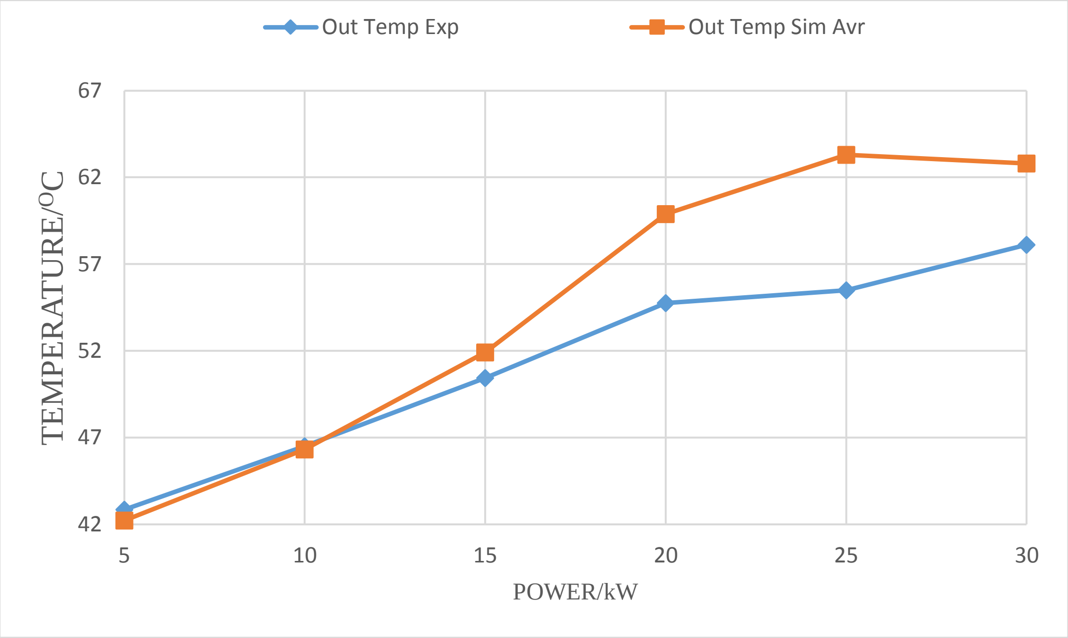

Figure 4.4 b: Graph of outlet Temperature versus Power for averaged channel

In Figures 4.4a and 4.4b, the result of increasing the mass flow rate for 30 kW for the same condition led to a reduction on the deviation observed for 30 kW data point in Figure 4.3a and 4.3b.

The observed effect of varying mass flow rate for the simulation at 30 kW informed the need to also increase the mass flow rates for the simulation at 20 kW to 30 kW. Figures 4.5a and 4.5 b shows plots of temperature against power obtained after varying the mass flow rate for the simulation at 20 kW and 25 kW from 0.15 kg/s to 0.18 kg/s and 0.20 kg/s respectively. The simulation at 30 kW was also further increased from 0.20 kg/s to 0.23 kg/s.

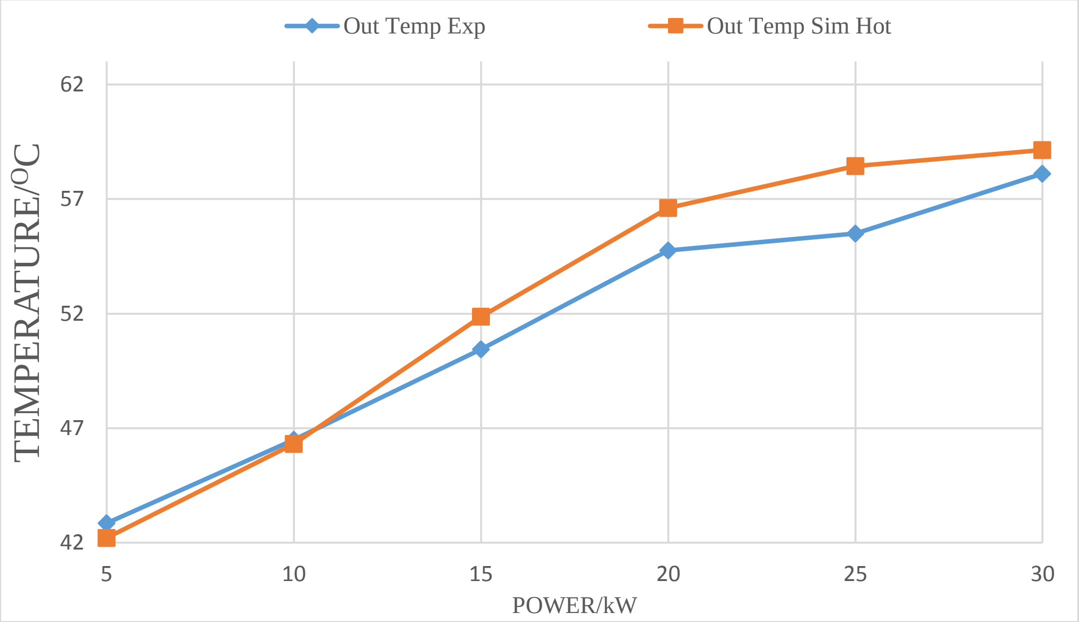

Figure 4.5 a: Graph of outlet Temperature versus Power for hottest channel

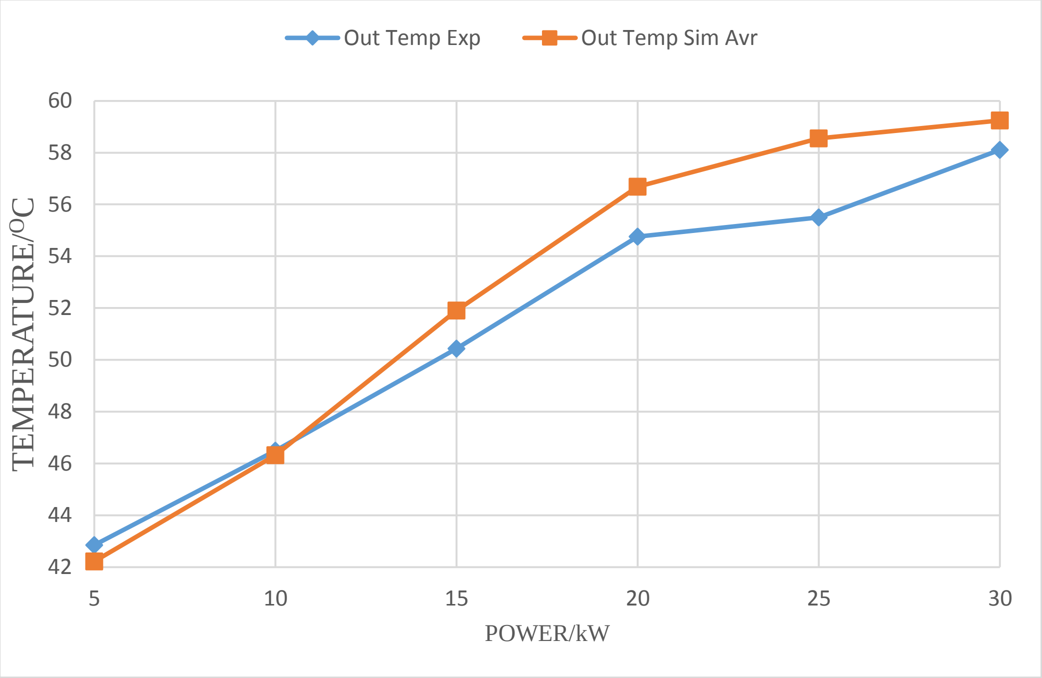

Figure 4.5 b: Graph of outlet Temperature versus Power for averaged channel

The result in Figure 4.5a and 4.5b show a significant reduction in the deviation of the data points for 20 kW to 30 kW and therefore, the data obtained from the simulation show a better agreement with the experimental. It is found that increasing mass flow rate enhances the heat transfer rate leading to a decrease in the outlet temperature. The effect of mass flow rate on outlet temperature is presented in Table 4.1.

Table 4.1: Mass flow rate on outlet temperature at 30 kW

mass flow rate	T_{exp}	T_{hot}	T_{avr}	$T_{hot} - T_{exp}$	$T_{avr} - T_{exp}$	$T_{hot} - T_{avr}$
0.15	58.11	73.17	73.57	15.06	15.46	0.4
0.20	58.11	62.63	62.80	4.52	4.69	0.17
0.23	58.11	59.14	59.24	1.03	1.13	0.10

When the mass flow rate for 30 kW was increased from 0.15 kg/s to 0.23 kg/s, the difference between the experimental outlet temperature and the simulation outlet temperature decreased for both averaged and hottest channels as presented is Table 4.1.

For 34.8% increase in the mass flow rate, the percentage decrease in temperature between the hottest channel and the experimental data was found to be 93.2% while that between the averaged channel and the experimental data was 92.7%. The decrease in temperature between the hottest channel and averaged channel was also found to be 75%. The percentages were calculated using equations 4.1 and 4.2.

$$\frac{(T_{hot} - T_{ext})_{0.15} - (T_{hot} - T_{ext})_{0.23}}{(T_{hot} - T_{ext})_{0.15}} \qquad (4.1)$$

$$\frac{(T_{avr} - T_{ext})_{0.15} - (T_{avr} - T_{ext})_{0.23}}{(T_{avr} - T_{ext})_{0.15}} \qquad (4.2)$$

where,

T_{ext} = experimental outlet temperature

T_{avr} = Simulation outlet temperature for the averaged channel

T_{hot} = Simulation outlet temperature for the hottest channel

It is observed that a very close agreement with the experimental data will be obtained by further increasing the mass flow rate for the simulation at 20 kW to 30 kW. Generally, the trend of the simulation plots show that as power increases, there is a build-up of heat within the core. Hence there is need to allow more coolant into the system for efficient heat removal. STAR-CCM$^+$ CFD code is able to predict heat transfer and distribution in the core of GHARR-1 at the power levels considered.

4.3 DISTRIBUTION OF WALL Y+ IN THE DOMAIN

The wall y+ was taken as an average over each segment and plotted against power. The evaluated result is presented in Figure 4.6. The all y+ wall treatment was chosen for the adopted k-e model. The all y+ wall treatment was employed due to its versatility to give reasonable results on coarse meshes for y+ > 30 and on fine meshes for y+ ≤ 1 [27].

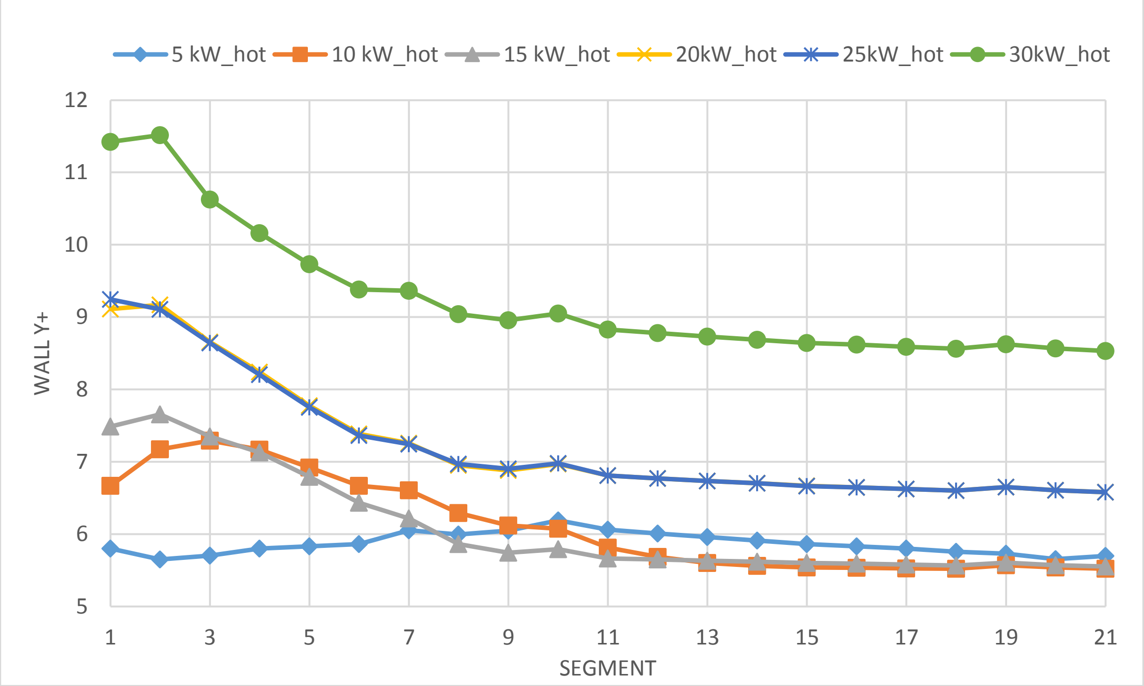

Figure 4.6: Wall y+ distribution over the domain.

For all power levels the wall y+ value decreases progressively along the flow channel and has its lowest value at the outlet. From the graph wall y+ increases with increasing power this is due to its dependence on density, velocity and kinematic viscosity as presented in equation 4.3. The dimensionless wall y+ is related to the wall distance y from the prism layer cell by equation 4.3

$$y+=\frac{y}{v}\sqrt{\frac{\tau_w}{\rho}} \qquad (4.3)[27]$$

Where, τ_w is the wall shear stress, ρ is the density and v is the kinematic viscosity.

4.4 SURFACE AVERAGE TEMPERATURE

Surface average temperatures was obtained as an average over each segment. "SAT 5kW_Hot and SAT 5kW_Avr" used in the legend are abbreviations for surface average temperature taken over each segment for the simulation at 5 kW for the hottest channel and averaged channel respectively. Figure 4.7 a. and 4.7 b. show the variation of the surface temperature with position for hottest channel and averaged channel respectively.

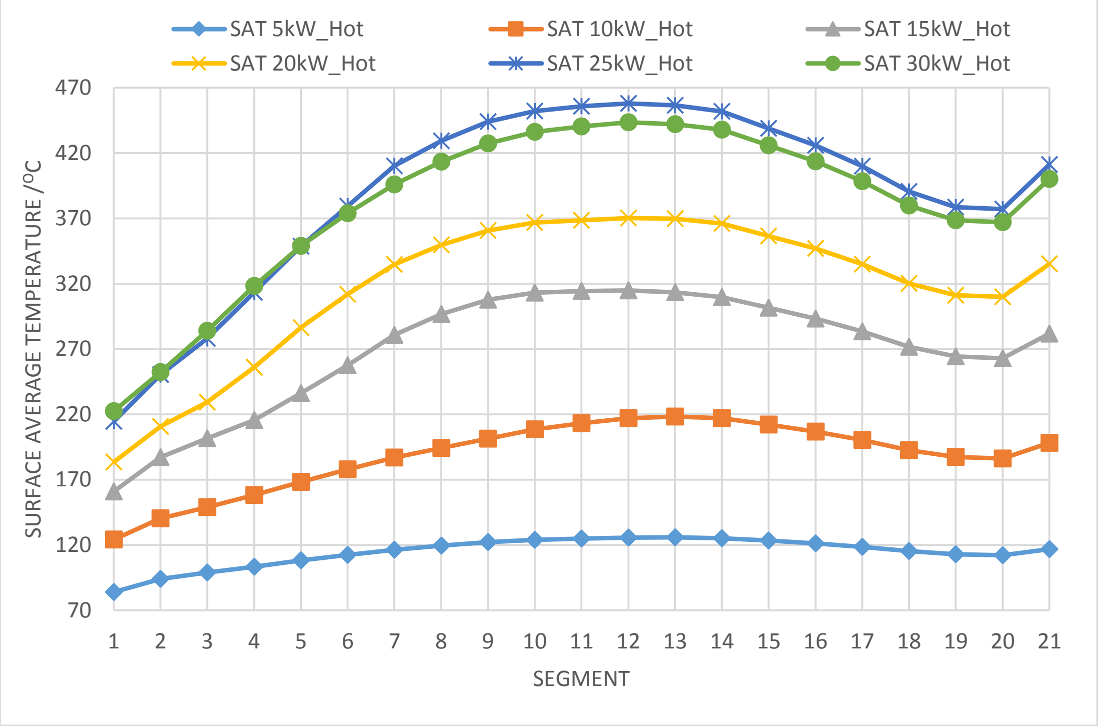

Figure 4.7 a: Surface Average Temperature versus Position for hottest channel

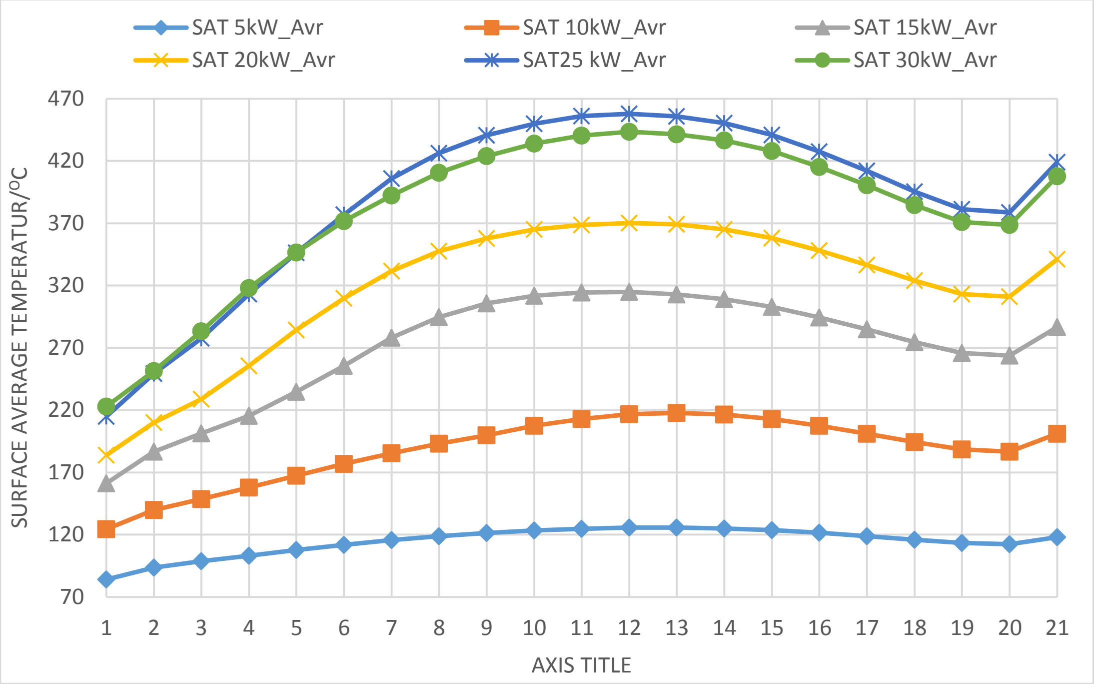

Figure 4.7 b: Surface Average Temperature versus Position for averaged channel

The result shows that the surface average temperature increases with increase in power. For both hottest and averaged channels, the surface average temperatures are lowest at the inlet and peaks at a value at the 12th segment. For all powers, the peak experienced a steady decrease from segment 14 to 19 before rising at segment 20. The lowest surface temperature is recorded for the simulation 5 kW in both hottest and averaged channels. Table 4.2 presents an evaluation on the trend difference for power level consideration.

Table 4.2: surface temperature for varying power levels.

Power (kW)	Segment 1 surface temperature	Change in temperature
30	222.8	
25	215.1	7.7
20	183.7	31.4
15	161.3	22.4
10	124.4	36.9
5	84.1	40.3

From the table 4.3, the least difference in the trends exist between trends for simulation at 30 kW and 25 kW. This result is in agreement with the result of local distribution of surface temperatures previously recorded [1] where the local surface temperature increases with the increase in the heat flux. In addition, with the local surface temperature increasing towards the outlet of the channel.

4.5 BULK AVERAGE TEMPERATURE

The fluid bulk average temperature was taken over each segment with the aid of constraint planes placed at the inlet and outlet. This is done to determine the temperature distribution within the fluid. Figure 4.8 a. and 4.8 b. shows variation of bulk average temperature with position taken over each segment for hottest and averaged channels respectively. "BAT 5kW_Hot and BAT 5kW_Avr" used in the legend are abbreviations for fluid bulk average temperature taken over each segment for the simulation at 5 kW for the hottest channel and averaged channel respectively.

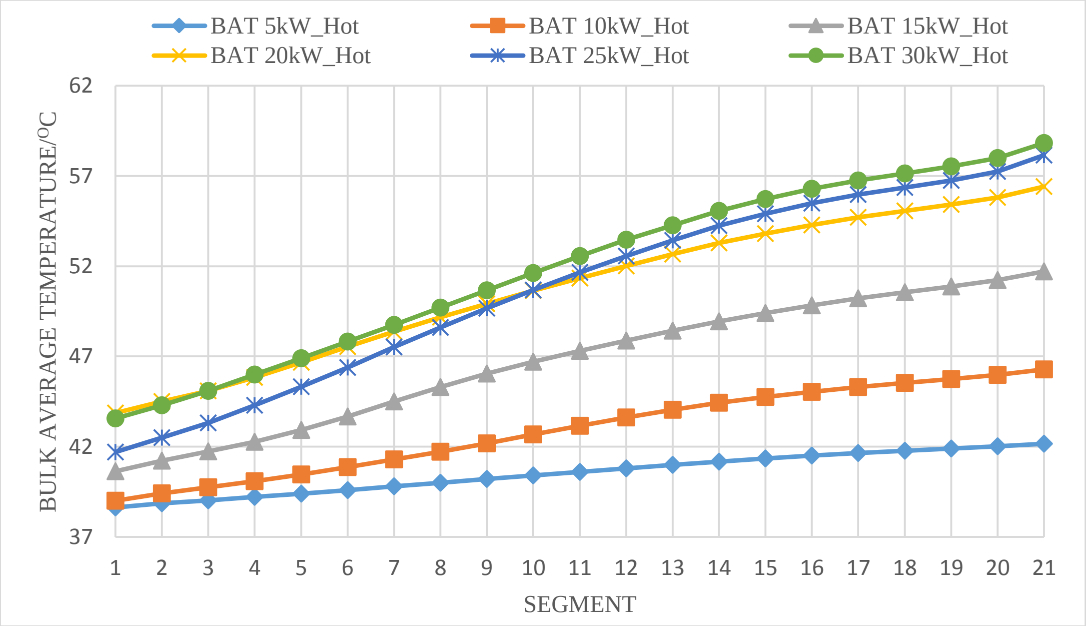

Figure 4.8 a: Bulk Average Temperature versus Position for hottest channel

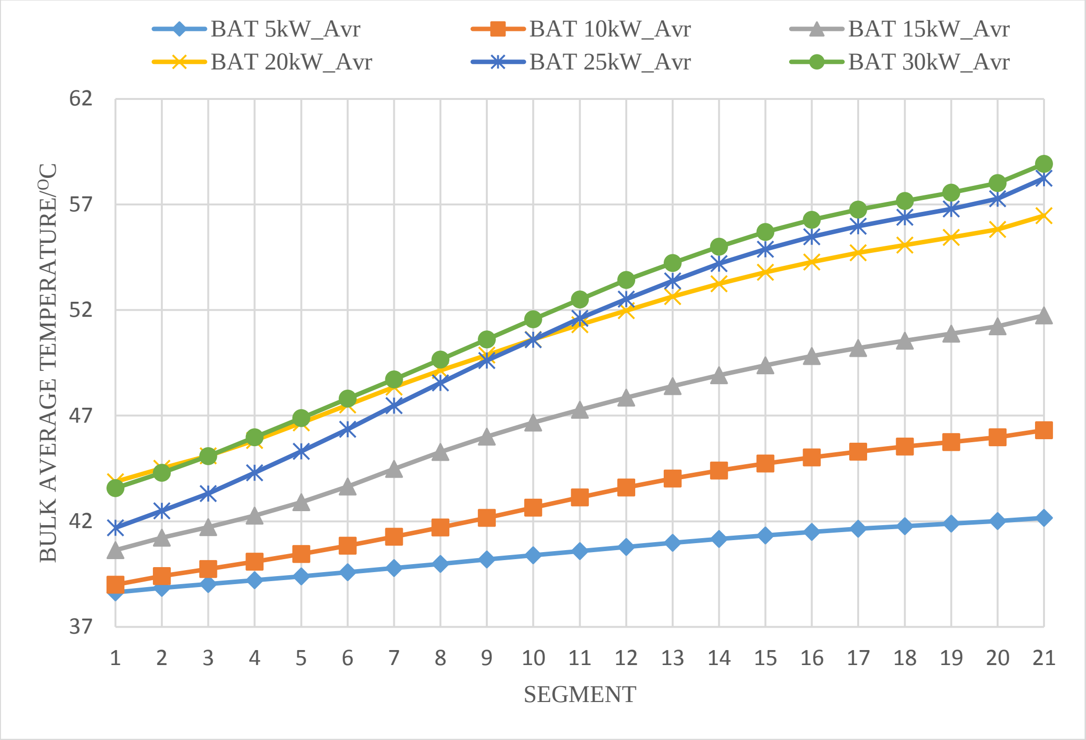

Figure 4.8 b: Bulk Average Temperature versus Position for averaged channel

The general trend shows an increase in the fluid temperature along the channel. It also shows greater variation in the temperature along the channel with a maximum variation at the exit. This suggest that as the fluid moves upwards in the channel more heat is extracted from the fuel. The trend is consistent for 5, 10, 15 and 20 kW powers but different for 25 and 30 kW due to increase in mass flow rate.

The trend for bulk average temperature conforms to that previously reported [1] where the local coolant temperature increases with the increase in the coolant inlet temperature. In addition, increase in the local coolant temperature along channel is higher close to the outlet of the channel.

4.6 SURFACE AND BULK TEMPERATURE COMPARISON

The surface average and fluid bulk average temperatures are compared in order to study the extent to which heat is extracted from the surface to the bulk of the fluid. Figures 4.9 shows a plot for surface average temperature and fluid bulk average temperature taken for the simulation at 15 kW for hottest channel.

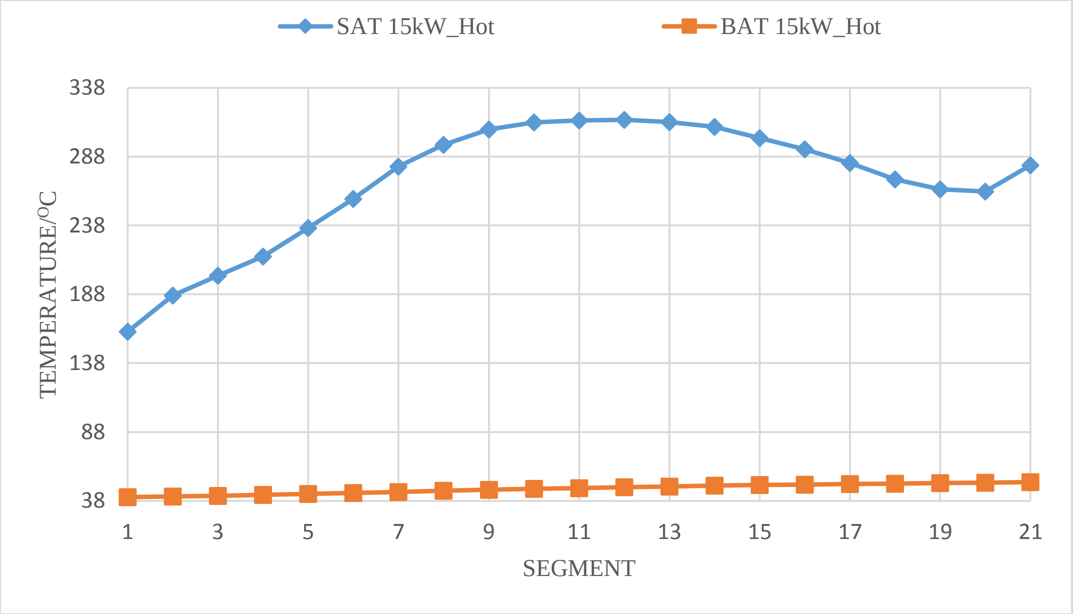

Figure 4.9: Surface and Bulk Temperature for hottest channel versus Position for 15kW

The result shows an increase in both the surface and fluid bulk average temperature from inlet to outlet. However, the trend for surface average temperature shows a sharp rise between segment 1 and 8 followed by a slight rise between segment 8 and 11. Between segment 11 and 19 the trend is a downwards curve followed by another rise between segment 20 and 21. The temperature on the surface is due to the applied heat on the wall surface. The resulting fluid bulk temperature suggests that the heat is conducted in such a way that the fluid bulk temperature remain in liquid phase two phase flow is attained. The resulting outlet temperature is within a range that can be cooled by natural convection. No correlation was observed between the surface average and the fluid bulk average temperature trends.

However addition of 7 line probes between the surface and the fluid centerline gives a correlated temperature distribution presented in Figure 4.10. The number in the parenthesis in the legend gives the distance of the probe point from the fluid centerline.

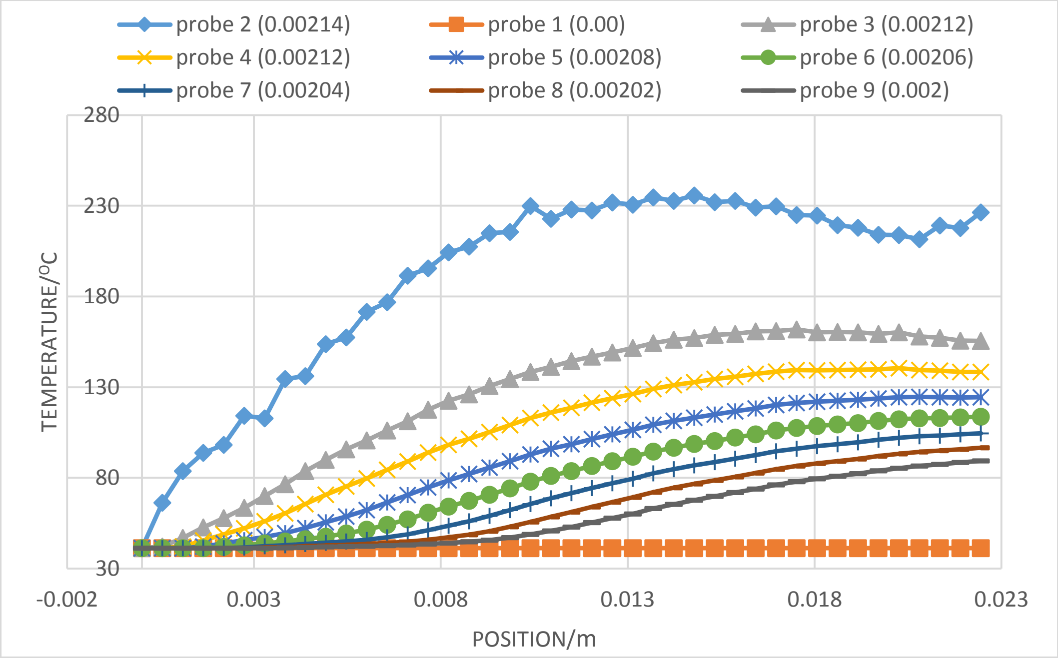

Figure 4.10: Temperature distribution trend close to boundary layer

The result shows the temperature increasing along the channel from inlet to outlet. The trend shows the curve flattening from the surface to the fluid centerline. Temperature distribution at the boundary layer is greatest at the wall where the heat flux is applied.

4.7 BULK AVERAGE TURBULENT INTENSITY

The fluid bulk turbulent intensity was calculated as an average over each segment to investigate the degree of turbulence in the various segments of the GHARR-1 core. The turbulent intensity was computed using equations 4.3 and 4.4 and the results evaluated are plotted in Figures 4.11a and 4.11b.

$$I = \frac{\acute{\upsilon}}{\tilde{v}} \qquad (4.3)$$

where $\tilde{v}$ is the mean flow velocity (computed using Appendix D) and

$$\acute{\upsilon} = \sqrt{\frac{2}{3}k} \qquad (4.4)$$

where k is the turbulence kinetic energy (Appendix C).

Figures 4.11a and 4.11b show a graph of turbulent intensity versus position for hottest and averaged flow channels respectively. “TI 5kW_hot and TI 5kW_avr” used in the legend are abbreviations for turbulent intensity taken over each segment for the simulation at 5 kW for the hottest channel and averaged channel respectively.

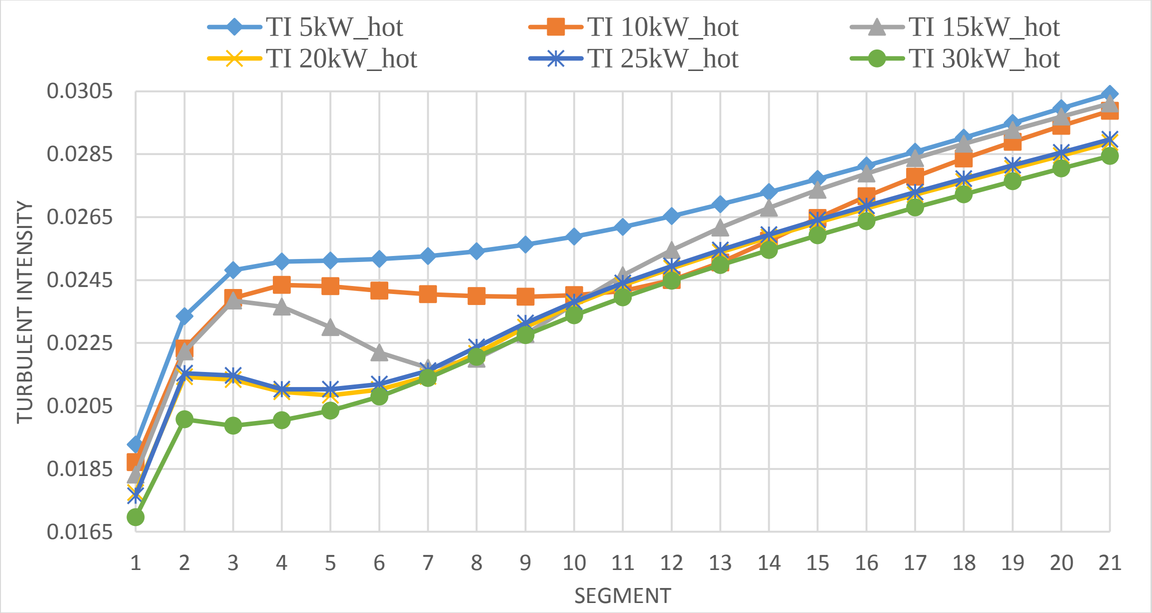

Figure 4.11a: Bulk Average Turbulent Intensity versus Position for hottest channel

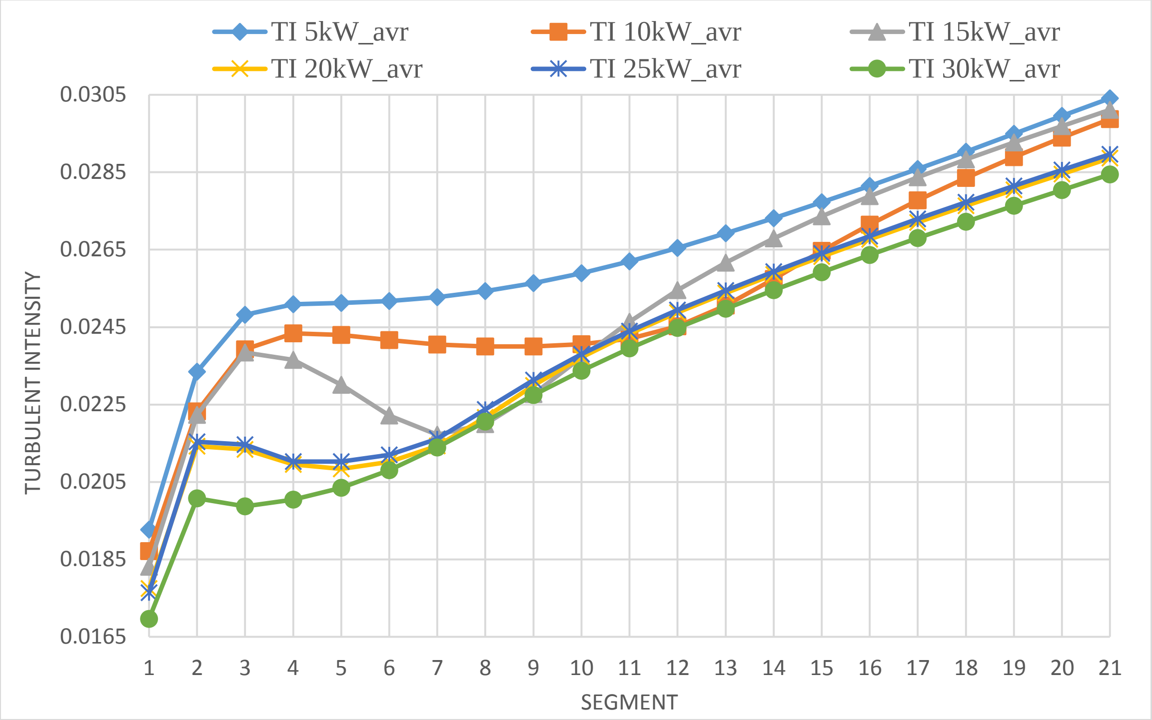

Figure 4.11b: Turbulent Intensity versus Position for averaged channel.

The turbulence values recorded at the inlet segment increased sharply between segments 1 and 2 for simulations at 15 kW to 30 kW. Between segments 3 and 7, turbulence intensity values decreased for the simulations at 15 kW to 30 kW. The sharp increase and subsequent decrease in turbulent intensity observed between segments 1 and 7 could be attributed to the initiation of flow development in the channel. From the 7th segment, steady rise in turbulence intensity was observed through to the exit of the domain. The development of the flow from the 7th segment could be said to be more appreciable than that observed between segments 1 and 7.

The turbulent intensity observed at lower powers of 5 kW and 10 kW were higher in magnitude than those observed at 15 kW to 30 kW. This is as a consequence of the inverse proportionality relationship existing between turbulent intensity and velocity. Hence the higher coolant velocities obtained at higher powers of 15 kW to 30 kW contributed to the lower turbulent intensities and vice versa.

4.8 CHANNEL CENTERLINE PRESSURE

The channel centerline pressure was taken using a line probe placed at the center of the geometry to analyze trend of the pressure across the domain. Figures 4.12a and 4.12b show the plot of fluid centerline pressure versus position for simulation at 5 kW to 30 kW for average and hottest channel respectively. “Pres 5kW_Hot and Pres 5kW_Avr” used in the legend are abbreviations for channel centerline pressure taken over each segment for the simulation at 5 kW for the hottest channel and averaged channel respectively.

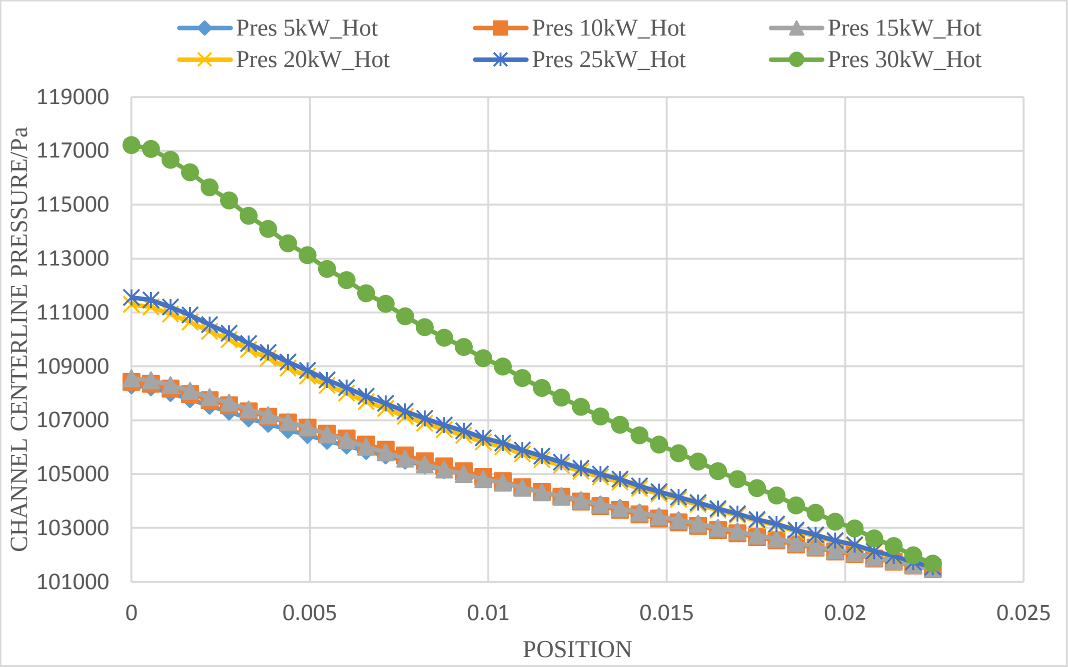

Figure 4.12 a: Fluid Centerline Pressure versus Position for hottest channel

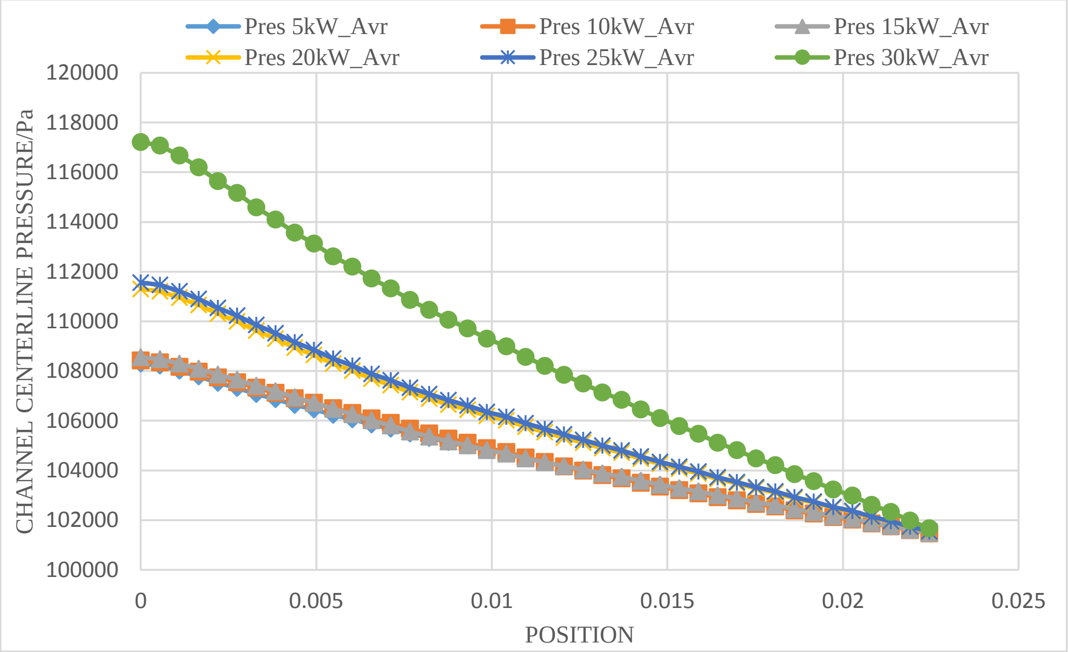

Figure 4.12 b: Fluid Centerline Pressure versus Position for averaged channel

The pressure at the inlet gives the required pressure for system start-up. The trends show that inlet pressure needed increases with increasing power. The difference between the inlet and outlet pressure for specified power level presented in Figure 4.12a and 4.12b gives the required pressure drop needed to push the fluid from inlet to outlet. The computed pressure drop for specified mass flow rates imposed on the simulation at 30 kW power for hottest channel is presented in Table 4.3.

Table 4.3: Mass flow rate and pressure drop for 30 kW power

Mass flow rate	Outlet pressure	Inlet pressure	Pressure drop
0.15	101493.2	109299.8	7806.6
0.2	101592.6	113884.7	12292.1
0.23	101671.4	117213.3	15541.9

Table 4.3 shows that an increase in mass flow rate lead to increase in the corresponding pressure drop required to push the fluid out of the system.

4.9 CONTOUR PLOTS FOR HOTTEST CHANNEL SIMULATION AT 30 kW

Contour plots are presented over constrained planes in other to visualise the heat transfer and distribution from the surface to the bulk fluid at different positions in the domain. The plots taken at inlet, outlet and middle segments are presented in Figures 4.13 to 4.15.

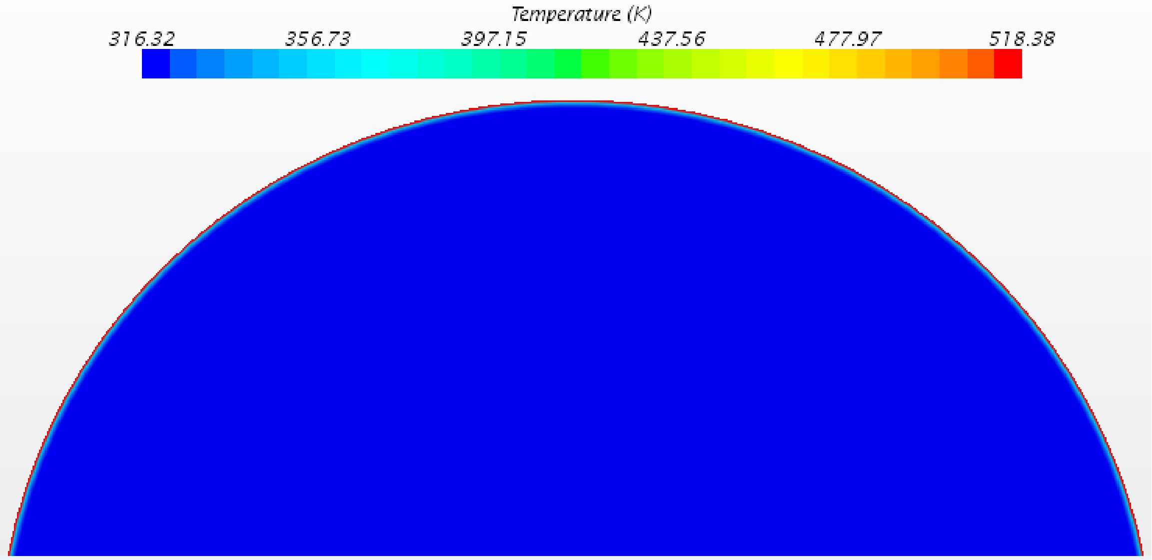

Figure 4.13: Inlet segment temperature distribution

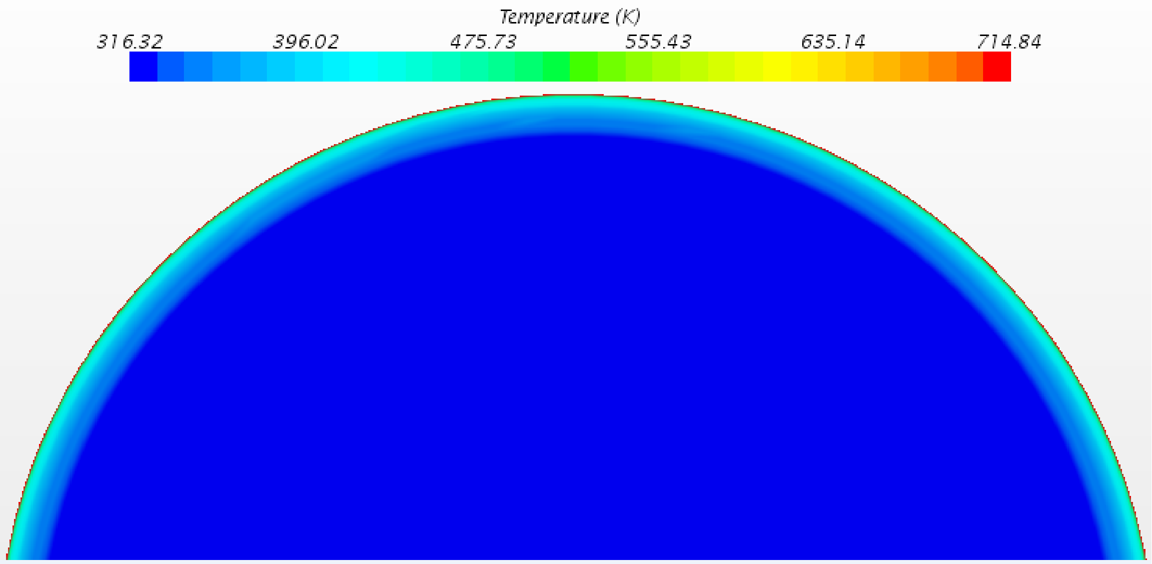

Figure 4.14: Temperature distribution in the middle segment

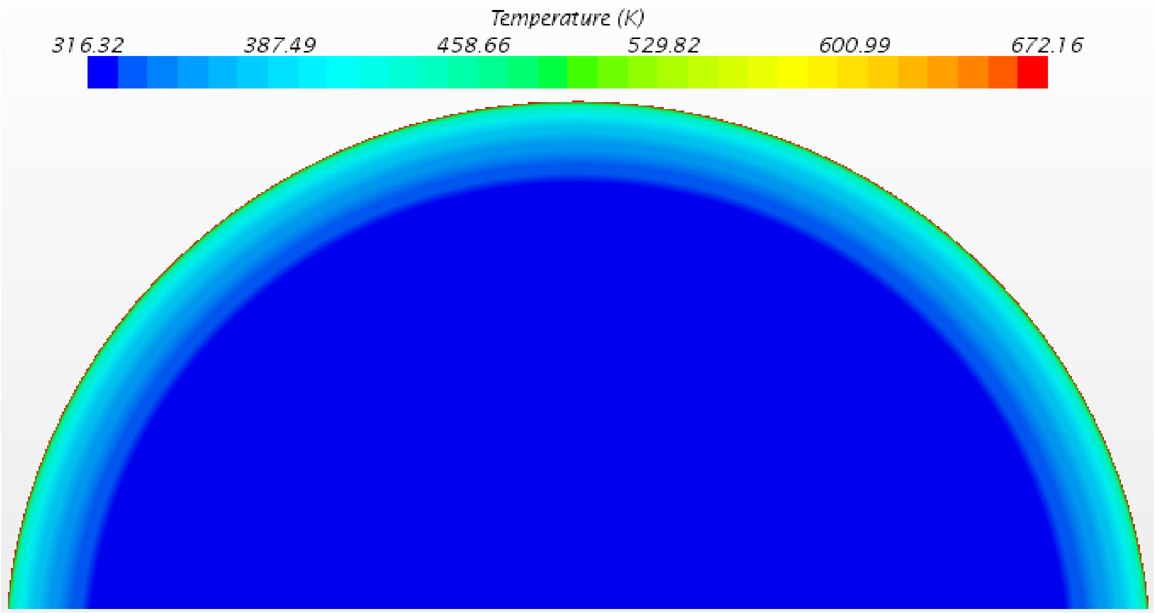

Figure 4.15: outlet segment temperature distribution

Figure 4.13 shows a uniform distribution of temperature over the interface. The interface temperature was observed to be the same as the inlet temperature. Figure 4.14: shows an decrease in temperature from the surface to the bulk of the fluid. It also shows the effectiveness of the coolant to remove heat from the fuel rod surface. This can be seen in the manner at which high surface temperature is removed without heating the bulk of the fluid. Compared to Figure 4.13, there is a build of temperature at the region around the wall boundary in Figure 4.14. Figure 4.15 shows a boundary temperature development of greater magnitute than those observed in Figures 4.13 and 4.14. This implies that the temperature close to the walls increases along the domain.

The contour plot of domain surface temperature shows temperature distribution on the surface of the flow channel. Figure 4.16 gives the contour plot for domain surcae temperature.

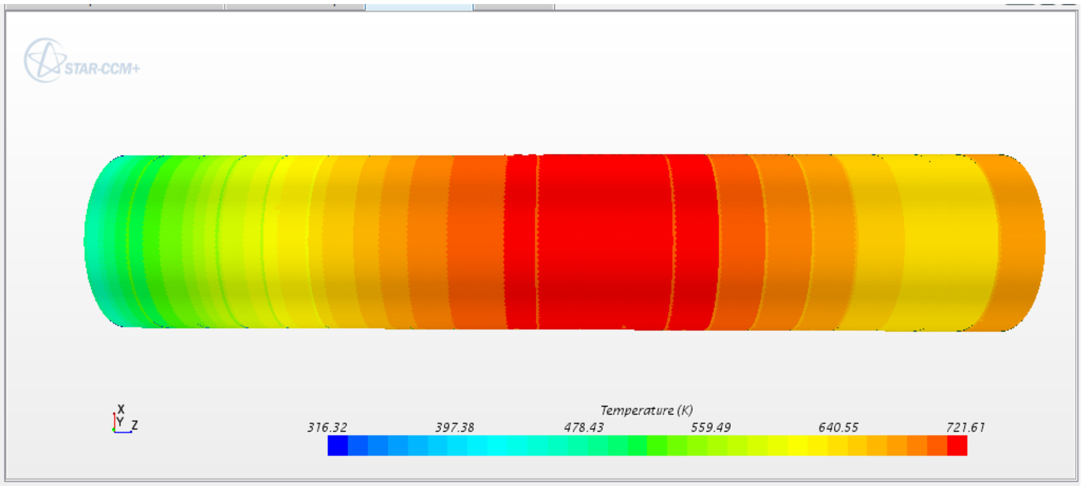

Figure 4.16: Surface temperature distribution

The contour shows the surface temperature is least between segment 1 and 9 peaking at the middle of between segment 10 and 15 before dropping to a lesser temperature between segment 16 and 21. The surface temperature distribution follows the same trend as the power peaking factors presented in Table 3.3.

4.10 COEFFICIENT OF HEAT TRANSFER

The coefficient of heat transfer was calculated for each segment using equations 4.5 and 4.6. The result of the evaluated heat transfer coefficient is plotted against the segment as presented in Figure 4.17.

$$h = \frac{q}{A_s \Delta T} \qquad (4.5).$$

$$\Delta T = T_s - T_b \qquad (4.6)$$

where A_s is the surface area, q is segmental power, T_s is surface temperature, T_b is the bulk temperature

Figure 4.17 gives a plot of coefficient of heat transfer against segment for simulations at 30 kW. “CHT_30kW hot and CHT_30kW avr” used in the legend are abbreviations for coefficient of heat transfer for hottest and averaged channels respectively.

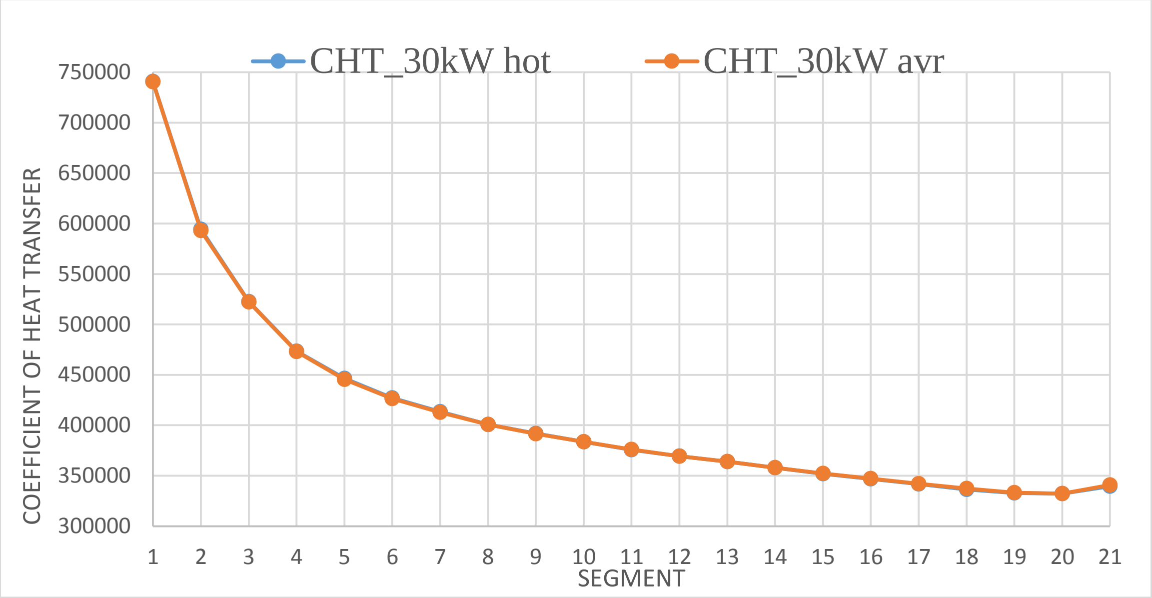

Figure 4.17: Coefficient of heat transfer versus Position

The trend shows the highest heat transfer coefficient exist at segment 1 followed by a progressive reduction up to segment 20 before a slight rise between segment 20 and 21.

Findings of the analysis performed for heat transfer and distribution in GHARR-1 core has been presented. Conclusion on the above discussed results will be drawn in the next Chapter.

CHAPTER FIVE

CONCLUSION AND RECOMMENDATION

5.1 CONCLUSION

A study of heat transfer and distribution was conducted to evaluate the steady state thermal hydraulic behavior of GHARR-1 core under natural convection cooling. Based on the results obtained, significant conclusion are hereby drawn:

1) The surface average temperature increases along the flow channel from inlet to outlet but peaks at the middle segments in conformity with the trends of GHARR-1 power peaking factors presented in Table 3.3.
2) The fluid bulk average temperature increases along the flow channel. A sharp increase in fluid bulk temperature was observed between segment 1 and 12. However between segment 12 and 21 the rate of increase in temperature dropped slightly. This suggests that, as the fluid develops, more heat is taken from the fuel and transported towards the outlet. It was also observed that the fluid bulk temperature increases with increase in power.

   However lateral distribution of temperature from the surface to the fluid centerline shows an effective heat transfer through the fluid.
3) There is a general increase in the turbulent intensity over the domain from inlet to outlet which also increases with increase in power. This suggest that as the flow develops, there is a build-up of turbulence in the domain. The observed trends suggests a turbulence surge at the inlet accompanied by a turbulence drop while the fluid stabilizes before an even greater rise in turbulent intensity. This observation

conforms to GHARR-1 Safety Analysis that the closer the coolant gets to the upper part of the fuel elements, the stronger the turbulence becomes [8].

4) The fluid centerline pressure was found to increase with increase in power, this suggest that both the required pressure for starting the system and the required pressure drop for transporting the fluid across the domain increases with power increase.
5) The values of outlet temperature for experimental measurements are lower than those calculated by STAR-CCM+ CFD code by a deviation of 1% - 1.6%. With this variation, taking into consideration meshing model dynamics, it is concluded that STAR CCM+ has predicted the studied physical parameters.
6) The present study has predicted the trend of the measured parameters as fluid develops from inlet to outlet of modified GHARR-1 core. This provides more insight about the distribution of mean and turbulent flow parameters for GHARR-1 core.
7) The failure to predict power beyond 31.2 kW in PLTEMP/ANL transient analysis in [7] informed the need to restrict the present steady state studies to 30 kW power level. The results from the present steady state reaffirms those obtained from the PARET/ANL transient simulations which indicates that Ghana Research Reactor-1 is safe to operate at the at a nominal power of 30 kW.

5.2 RECOMMENDATIONS

The present work should be extended to include thermal hydraulics study of GHARR-1 core subchannel to enable a more general conclusion on heat transfer and distribution. Also other CFD codes should be studied using the same conditions as the present study for verification. A full geometry of GHARR-1 core should be modelled and simulated using STAR-CCM+ for heat transfer analysis with the view of updating GHARR-1 Safety Analysis Report book. The present work should be extended to study GHARR-1 core heat transfer and distribution during accident and transient conditions.

REFERENCES

[1] Talha K. A., Acbdel-Hadi E. A., El-Ghnam R. I., Taher S. H. and Abdel-Latif S. H. (2012). Thermal Hydraulic Behavior of Research Reactor during Natural Convection Cooling Mode. Arab Journal of Nuclear Science and Applications, 45:4 243-256**.**

[2] Annafi T. A., Gyeabour A. A., Akaho E. H. K., Annor-Nyarko M. and Quaye C. R. (2014). Finite Difference Analysis of the Transient Temperature Profile within Gharr-1 Fuel Element. International Journal of Scientific and Technology Research. 3:8 2277-8616.

[3] Akaho E.H.K., Maaku B.T., Anim Sampong S., Emi-Reynolds G, Boadu H.O, , Dodoo-Amoo D.N.A. (2006). Ghana Research Reactor-1, Final Safety Analysis Report. GAEC, Kwabenya, Ghana.

[4] Sogbadji R. B.M**.** (2012). Neutronic Study of the Mono-Recycling Of Americium in PWR and Of the Core Conversion in MNSR Using the Mure Code. Research Thesis submitted to Universite De Paris Sud.

[5] Odoi H., Akaho E. H. K., Anim-Sampong S., Jonah, Nyarko, S. B. Abrefah R., Ampomah-Amoako E., Sogbadji R B. M., Lawson I., Birinkoranga S., Ibrahimc Y. and Boffie J. (2011). Investigative studies on effect of reflector thickness on the performance of low enriched uranium-fuelled MNSR’s. Nuclear Engineering and Design 241:8 2902-2915.

[6] Sogbadji R B M., Abrefah R., Ampomah-Amoako, E Agbemava. S. and Nyarko B. J.B. (2011). Neutron energy spectrum flux profile of Ghana’s miniature neutron source reactor core. Annals of Nuclear. Energy 38:8 1787-1792.

[7] Ampomah-Amoako E., Akaho E.H.K., Anim-Sampong S., Nyarko B.J.B. (2009). Transient Analysis of Ghana Research Reactor-1 using PARET/ANL thermal–hydraulic code. Nuclear Engineering and Design 239: 2479–2483.

[8] Akaho E.H.K., Maakuu B.T., Anim-Sampong S., Emi-Reynolds G., Boadu H.O., Osae E.K., Akoto S. B., Dodoo-Amoo D.N.A. (2003). Ghana Research Reactor-1 Safety Analysis Report. GAEC-NNRI-RT-90

[9] Lienhard IV J. H, Lienhard V J. H. (2008). A Heat Transfer Textbook, third edition. Phlogiston Press, Cambridge, Massachusetts, USA p 137

[10] https://en.wikipedia.org/wiki/Natural_convection 17/04/20015

[11] http://encyclopedia2.thefreedictionary.com/single-phase+flow 24/03/2015

[12] Akaho E. H. and Maaku B. T. (2002). Simulation of transients in a miniature neutron source reactor core. Nuclear Engineering and Design. 213:1 31-42

[13] Appiah R. (2011). Steady State Thermal-Hydraulics Analysis of GHARR-1 using the PL TEMP/ANL v4.0 Code. University of Ghana, Accra, Ghana.

[14] Costa A. L., Reis P. A. L., Silva C. A. M., Pereira C., Veloso M. A. F., Guerra B. T., Soares H. V. and Mesquita A. Z. (2011). Safety Studies and General Simulations of Research Reactors Using Nuclear Codes, Nuclear Power - System Simulations and Operation, Dr. Pavel Tsvetkov (Ed.),

[15] Böck H. and Villa M. (2001). Survey of Research Reactors, prepared for the IAEA Course on "Safety, Management and Utilization of Research Reactors". Bratislava-Vienna.

[16] Sunniva S. T. (2013). Simulation of Viscous Flow around a Circular Cylinder with STAR-CCM+. A Master's Degree Thesis submitted to the Norwegian University of Science and Technology, Department of Marine Technology

[17] Ganesh V. (2012). Understanding CFD Simulation Process with Examples https://ganeshvisavale.wordpress.com/2012/12/07/understanding-cfd-simulation-process-with-examples/

[18] STAR-CCM+ User Guide version 6.04.014 CD_ADAPCO 2011.

[19] Versteeg H. K., Malalasekera, W. (2007). An Introduction to Computational Fluid Dynamics, the Finite Volume Method. Second edition, pp. 54-128.

[20] Ampomah-Amoako E. (2013). Stability and control of Supercritical Water Reactor System; A Study into Concepts and Applications. A Nuclear Engineering Ph.D. Dissertation Submitted to the University of Ghana

[21] Spalart P. R., and Rumsey C.L. (2007). Effective Inflow Conditions for Turbulence Models in Aerodynamic Calculations, AIAA Journal, 45:10 2544-2553

[22] Henkes R.A.W.M., Vander-Flugt F. F., Hoohendoorn C. J. (1991). Natural convection in a square cavity calculated with low-Reynolds number turbulence models. Int. J. Heat Mass Transfer, 34: 1543-1557

[23] Okon C. E., Chad-Umoren Y. E. and Abbey T. M. (2013). Thermal Profile of Cylindrical Nuclear Reactor Fuel Elements “An Analytical Approach” Canadian Journal on Computing in Mathematics, Natural Sciences, Engineering and Medicine 4:1

[24] Kyei A.Y., Annafi T. A., Annor-Nyarko M, Quaye C. R, Bansah C. (2014). Modelling the Velocity Profile of Coolant Flow in the GHARR-1 Fuel Channel. Journal of Nuclear Energy Science and Power Generation Technology http://dx.doi.org/10.4172/2325-9809.1000123

[25] Ampomah-Amoako E., Akaho E. H.K. , Nyarko B. J.B. , Ambrosini W. (2013). Analysis of flow stability in nuclear reactor subchannels with water at supercritical pressures. Annals of Nuclear Energy 60: 396–405

[26] The NIST Reference on Constants, Units, and Uncertainty http://physics.nist.gov/cuu/Units/units.html

[27] Agbodemegbe V.Y., Cheng X, Akaho E.H.K, Allotey F.K.A. (2015). Correlation for Cross-Flow Resistance Coefficient Using STAR-CCM+ Simulation Data for Flow of Water through Rod Bundle Supported by Spacer Grid with Split-Type Mixing Vane. Nuclear Engineering and Design 285: 134–149.

APPENDIX

APPENDIX A

Table 6.1: Thermophysical Properties

Temperature (^{o}C)	Density (kg/m3)	Viscosity (Pa*s)	Therm. Cond. (W/m*K)	mass fl. rate (kg/s)
1	9.999E+02	1.731E-03	5.630E-01	1.110E-01
2	9.999E+02	1.673E-03	5.649E-01	1.110E-01
3	1.000E+03	1.619E-03	5.668E-01	1.110E-01
4	1.000E+03	1.567E-03	5.687E-01	1.110E-01
5	1.000E+03	1.518E-03	5.706E-01	1.110E-01
6	9.999E+02	1.471E-03	5.725E-01	1.110E-01
7	9.999E+02	1.427E-03	5.744E-01	1.110E-01
8	9.999E+02	1.385E-03	5.763E-01	1.110E-01
9	9.998E+02	1.344E-03	5.782E-01	1.110E-01
10	9.997E+02	1.306E-03	5.801E-01	1.110E-01
11	9.996E+02	1.269E-03	5.819E-01	1.110E-01
12	9.995E+02	1.234E-03	5.838E-01	1.109E-01
13	9.994E+02	1.200E-03	5.857E-01	1.109E-01
14	9.993E+02	1.168E-03	5.875E-01	1.109E-01
15	9.991E+02	1.138E-03	5.894E-01	1.109E-01
16	9.990E+02	1.108E-03	5.912E-01	1.109E-01
17	9.988E+02	1.080E-03	5.931E-01	1.109E-01
18	9.986E+02	1.053E-03	5.949E-01	1.108E-01
19	9.984E+02	1.027E-03	5.967E-01	1.108E-01
20	9.982E+02	1.002E-03	5.985E-01	1.108E-01
21	9.980E+02	9.776E-04	6.002E-01	1.108E-01
22	9.978E+02	9.544E-04	6.020E-01	1.108E-01
23	9.975E+02	9.322E-04	6.038E-01	1.107E-01
24	9.973E+02	9.107E-04	6.055E-01	1.107E-01
25	9.971E+02	8.901E-04	6.072E-01	1.107E-01
26	9.968E+02	8.702E-04	6.089E-01	1.106E-01
27	9.965E+02	8.510E-04	6.106E-01	1.106E-01
28	9.962E+02	8.325E-04	6.122E-01	1.106E-01
29	9.960E+02	8.146E-04	6.139E-01	1.106E-01
30	9.957E+02	7.974E-04	6.155E-01	1.105E-01
31	9.953E+02	7.807E-04	6.171E-01	1.105E-01
32	9.950E+02	7.646E-04	6.187E-01	1.104E-01
33	9.947E+02	7.490E-04	6.203E-01	1.104E-01
34	9.944E+02	7.339E-04	6.218E-01	1.104E-01
35	9.940E+02	7.193E-04	6.233E-01	1.103E-01
36	9.937E+02	7.052E-04	6.248E-01	1.103E-01

37	9.933E+02	6.915E-04	6.263E-01	1.103E-01
38	9.930E+02	6.783E-04	6.278E-01	1.102E-01
39	9.926E+02	6.654E-04	6.292E-01	1.102E-01
40	9.922E+02	6.530E-04	6.306E-01	1.101E-01
41	9.918E+02	6.409E-04	6.320E-01	1.101E-01
42	9.914E+02	6.292E-04	6.334E-01	1.100E-01
43	9.910E+02	6.178E-04	6.348E-01	1.100E-01
44	9.906E+02	6.068E-04	6.361E-01	1.100E-01
45	9.902E+02	5.961E-04	6.374E-01	1.099E-01
46	9.898E+02	5.857E-04	6.387E-01	1.099E-01
47	9.894E+02	5.755E-04	6.399E-01	1.098E-01
48	9.889E+02	5.657E-04	6.412E-01	1.098E-01
49	9.885E+02	5.562E-04	6.424E-01	1.097E-01
50	9.880E+02	5.469E-04	6.436E-01	1.097E-01
51	9.876E+02	5.378E-04	6.448E-01	1.096E-01
52	9.871E+02	5.290E-04	6.459E-01	1.096E-01
53	9.867E+02	5.204E-04	6.471E-01	1.095E-01
54	9.862E+02	5.121E-04	6.482E-01	1.095E-01
55	9.857E+02	5.040E-04	6.493E-01	1.094E-01
56	9.852E+02	4.961E-04	6.503E-01	1.094E-01
57	9.847E+02	4.884E-04	6.514E-01	1.093E-01
58	9.842E+02	4.809E-04	6.524E-01	1.092E-01
59	9.837E+02	4.735E-04	6.534E-01	1.092E-01
60	9.832E+02	4.664E-04	6.544E-01	1.091E-01
61	9.827E+02	4.594E-04	6.554E-01	1.091E-01
62	9.822E+02	4.527E-04	6.563E-01	1.090E-01
63	9.816E+02	4.460E-04	6.572E-01	1.090E-01
64	9.811E+02	4.396E-04	6.581E-01	1.089E-01
65	9.806E+02	4.333E-04	6.590E-01	1.088E-01
66	9.800E+02	4.271E-04	6.599E-01	1.088E-01
67	9.795E+02	4.211E-04	6.607E-01	1.087E-01
68	9.789E+02	4.152E-04	6.615E-01	1.087E-01
69	9.783E+02	4.095E-04	6.623E-01	1.086E-01
70	9.778E+02	4.039E-04	6.631E-01	1.085E-01
71	9.772E+02	3.984E-04	6.639E-01	1.085E-01
72	9.766E+02	3.931E-04	6.647E-01	1.084E-01
73	9.760E+02	3.879E-04	6.654E-01	1.083E-01
74	9.754E+02	3.827E-04	6.661E-01	1.083E-01
75	9.748E+02	3.777E-04	6.668E-01	1.082E-01
76	9.742E+02	3.729E-04	6.675E-01	1.081E-01
77	9.736E+02	3.681E-04	6.681E-01	1.081E-01
78	9.730E+02	3.634E-04	6.688E-01	1.080E-01
79	9.724E+02	3.588E-04	6.694E-01	1.079E-01

80	9.718E+02	3.544E-04	6.700E-01	1.079E-01
81	9.712E+02	3.500E-04	6.706E-01	1.078E-01
82	9.705E+02	3.457E-04	6.712E-01	1.077E-01
83	9.699E+02	3.415E-04	6.718E-01	1.077E-01
84	9.693E+02	3.374E-04	6.723E-01	1.076E-01
85	9.686E+02	3.333E-04	6.728E-01	1.075E-01
86	9.680E+02	3.294E-04	6.734E-01	1.074E-01
87	9.673E+02	3.255E-04	6.739E-01	1.074E-01
88	9.666E+02	3.218E-04	6.743E-01	1.073E-01
89	9.660E+02	3.180E-04	6.748E-01	1.072E-01
90	9.653E+02	3.144E-04	6.753E-01	1.071E-01

APPENDIX B:

TABLE 6.2: Heat Fluxes for Averaged Channel

Segments	HF 5KW	HF 10KW	HF 15KW	HF 20KW	HF 25KW	HF 30KW
1	5.54E+06	1.11E+07	1.66E+07	2.21E+07	2.77E+07	3.32E+07
2	5.12E+06	1.02E+07	1.54E+07	2.05E+07	2.56E+07	3.07E+07
3	5.19E+06	1.04E+07	1.56E+07	2.08E+07	2.59E+07	3.11E+07
4	5.37E+06	1.07E+07	1.61E+07	2.15E+07	2.68E+07	3.22E+07
5	5.57E+06	1.11E+07	1.67E+07	2.23E+07	2.79E+07	3.34E+07
6	5.76E+06	1.15E+07	1.73E+07	2.30E+07	2.88E+07	3.46E+07
7	5.91E+06	1.18E+07	1.77E+07	2.37E+07	2.96E+07	3.55E+07
8	6.03E+06	1.21E+07	1.81E+07	2.41E+07	3.01E+07	3.62E+07
9	6.10E+06	1.22E+07	1.83E+07	2.44E+07	3.05E+07	3.66E+07
10	6.12E+06	1.22E+07	1.84E+07	2.45E+07	3.06E+07	3.67E+07
11	6.08E+06	1.22E+07	1.82E+07	2.43E+07	3.04E+07	3.65E+07
12	6.01E+06	1.20E+07	1.80E+07	2.40E+07	3.00E+07	3.61E+07
13	5.87E+06	1.17E+07	1.76E+07	2.35E+07	2.94E+07	3.52E+07
14	5.69E+06	1.14E+07	1.71E+07	2.28E+07	2.85E+07	3.42E+07
15	5.47E+06	1.09E+07	1.64E+07	2.19E+07	2.73E+07	3.28E+07
16	5.20E+06	1.04E+07	1.56E+07	2.08E+07	2.60E+07	3.12E+07
17	4.91E+06	9.81E+06	1.47E+07	1.96E+07	2.45E+07	2.94E+07
18	4.60E+06	9.21E+06	1.38E+07	1.84E+07	2.30E+07	2.76E+07
19	4.35E+06	8.71E+06	1.31E+07	1.74E+07	2.18E+07	2.61E+07
20	4.30E+06	8.61E+06	1.29E+07	1.72E+07	2.15E+07	2.58E+07
21	4.96E+06	9.91E+06	1.49E+07	1.98E+07	2.48E+07	2.97E+07
Total	1.14E+08	2.28E+08	3.42E+08	4.57E+08	5.71E+08	6.85E+08

APPENDIX C

Table 6.3: Heat Fluxes for Hottest Channel

Segments	HF 5KW	HF 10KW	HF 15KW	HF 20KW	HF 25KW	HF 30KW
1	5.519E+06	1.104E+07	1.656E+07	2.208E+07	2.760E+07	3.311E+07
2	5.149E+06	1.030E+07	1.545E+07	2.060E+07	2.574E+07	3.089E+07
3	5.198E+06	1.040E+07	1.560E+07	2.079E+07	2.599E+07	3.119E+07
4	5.370E+06	1.074E+07	1.611E+07	2.148E+07	2.685E+07	3.222E+07
5	5.619E+06	1.124E+07	1.686E+07	2.248E+07	2.809E+07	3.371E+07
6	5.805E+06	1.161E+07	1.741E+07	2.322E+07	2.902E+07	3.483E+07
7	5.983E+06	1.197E+07	1.795E+07	2.393E+07	2.992E+07	3.590E+07
8	6.070E+06	1.214E+07	1.821E+07	2.428E+07	3.035E+07	3.642E+07
9	6.150E+06	1.230E+07	1.845E+07	2.460E+07	3.075E+07	3.690E+07
10	6.142E+06	1.228E+07	1.843E+07	2.457E+07	3.071E+07	3.685E+07
11	6.067E+06	1.213E+07	1.820E+07	2.427E+07	3.033E+07	3.640E+07
12	6.002E+06	1.200E+07	1.801E+07	2.401E+07	3.001E+07	3.601E+07
13	5.877E+06	1.175E+07	1.763E+07	2.351E+07	2.939E+07	3.526E+07
14	5.710E+06	1.142E+07	1.713E+07	2.284E+07	2.855E+07	3.426E+07
15	5.429E+06	1.086E+07	1.629E+07	2.172E+07	2.714E+07	3.257E+07
16	5.166E+06	1.033E+07	1.550E+07	2.066E+07	2.583E+07	3.100E+07
17	4.865E+06	9.730E+06	1.460E+07	1.946E+07	2.433E+07	2.919E+07
18	4.521E+06	9.043E+06	1.356E+07	1.809E+07	2.261E+07	2.713E+07
19	4.312E+06	8.624E+06	1.294E+07	1.725E+07	2.156E+07	2.587E+07
20	4.278E+06	8.556E+06	1.283E+07	1.711E+07	2.139E+07	2.567E+07
21	4.828E+06	9.656E+06	1.448E+07	1.931E+07	2.414E+07	2.897E+07
Total	1.141E+08	2.281E+08	3.422E+08	4.562E+08	5.703E+08	6.844E+08

APPENDIX D

TABLE 6.4: Segment Bulk Average Turbulent Kinetic Energy

SEGMENT	BATKE 5kW_Hot	BATKE 10kW_Hot	BATKE 15kW_Hot	BATKE 20kW_Hot	BATKE 25kW_Hot	BATKE 30kW_Hot
1	6.046E-02	5.713E-02	5.485E-02	7.447E-02	7.355E-02	1.112E-01
2	8.877E-02	8.128E-02	8.085E-02	1.085E-01	1.096E-01	1.557E-01
3	1.003E-01	9.341E-02	9.305E-02	1.076E-01	1.089E-01	1.526E-01
4	1.025E-01	9.664E-02	9.154E-02	1.037E-01	1.045E-01	1.551E-01
5	1.028E-01	9.632E-02	8.658E-02	1.027E-01	1.045E-01	1.600E-01
6	1.031E-01	9.524E-02	8.062E-02	1.045E-01	1.062E-01	1.671E-01
7	1.039E-01	9.434E-02	7.711E-02	1.086E-01	1.104E-01	1.767E-01
8	1.052E-01	9.384E-02	7.914E-02	1.162E-01	1.183E-01	1.880E-01
9	1.069E-01	9.373E-02	8.487E-02	1.250E-01	1.265E-01	1.999E-01
10	1.091E-01	9.413E-02	9.214E-02	1.331E-01	1.339E-01	2.111E-01
11	1.116E-01	9.518E-02	9.939E-02	1.400E-01	1.407E-01	2.216E-01
12	1.146E-01	9.792E-02	1.060E-01	1.463E-01	1.471E-01	2.315E-01
13	1.179E-01	1.024E-01	1.120E-01	1.523E-01	1.531E-01	2.410E-01
14	1.213E-01	1.082E-01	1.175E-01	1.581E-01	1.590E-01	2.503E-01
15	1.250E-01	1.143E-01	1.225E-01	1.638E-01	1.648E-01	2.595E-01
16	1.289E-01	1.203E-01	1.272E-01	1.694E-01	1.704E-01	2.686E-01
17	1.330E-01	1.259E-01	1.317E-01	1.750E-01	1.761E-01	2.775E-01
18	1.372E-01	1.312E-01	1.360E-01	1.805E-01	1.817E-01	2.864E-01
19	1.416E-01	1.362E-01	1.401E-01	1.860E-01	1.872E-01	2.951E-01
20	1.462E-01	1.410E-01	1.442E-01	1.914E-01	1.927E-01	3.038E-01
21	1.506E-01	1.456E-01	1.484E-01	1.970E-01	1.983E-01	3.126E-01

APPENDIX E

TABLE 6.5: Segment Bulk Average Velocity

SEGMENT	BAV 5kW_Hot	BAV 10kW_Hot	BAV 15kW_Hot	BAV 20kW_Hot	BAV 25kW_Hot	BAV 30kW_Hot
1	1.041E+01	1.042E+01	1.042E+01	1.252E+01	1.251E+01	1.600E+01
2	1.041E+01	1.042E+01	1.042E+01	1.252E+01	1.251E+01	1.600E+01
3	1.041E+01	1.042E+01	1.042E+01	1.253E+01	1.252E+01	1.601E+01
4	1.041E+01	1.042E+01	1.043E+01	1.253E+01	1.252E+01	1.601E+01
5	1.041E+01	1.042E+01	1.043E+01	1.253E+01	1.252E+01	1.601E+01
6	1.042E+01	1.042E+01	1.043E+01	1.254E+01	1.253E+01	1.602E+01
7	1.042E+01	1.042E+01	1.043E+01	1.254E+01	1.253E+01	1.603E+01
8	1.042E+01	1.042E+01	1.044E+01	1.254E+01	1.254E+01	1.603E+01
9	1.042E+01	1.042E+01	1.044E+01	1.255E+01	1.254E+01	1.604E+01
10	1.042E+01	1.043E+01	1.044E+01	1.255E+01	1.255E+01	1.604E+01
11	1.042E+01	1.043E+01	1.044E+01	1.255E+01	1.255E+01	1.605E+01
12	1.042E+01	1.043E+01	1.045E+01	1.256E+01	1.256E+01	1.605E+01
13	1.042E+01	1.043E+01	1.045E+01	1.256E+01	1.256E+01	1.606E+01
14	1.042E+01	1.043E+01	1.045E+01	1.256E+01	1.257E+01	1.607E+01
15	1.042E+01	1.043E+01	1.045E+01	1.257E+01	1.257E+01	1.607E+01
16	1.042E+01	1.044E+01	1.046E+01	1.257E+01	1.257E+01	1.608E+01
17	1.042E+01	1.044E+01	1.046E+01	1.257E+01	1.258E+01	1.608E+01
18	1.042E+01	1.044E+01	1.046E+01	1.258E+01	1.258E+01	1.608E+01
19	1.042E+01	1.044E+01	1.046E+01	1.258E+01	1.258E+01	1.609E+01
20	1.042E+01	1.044E+01	1.046E+01	1.258E+01	1.259E+01	1.609E+01
21	1.042E+01	1.044E+01	1.046E+01	1.258E+01	1.259E+01	1.610E+01

APPENDIX F

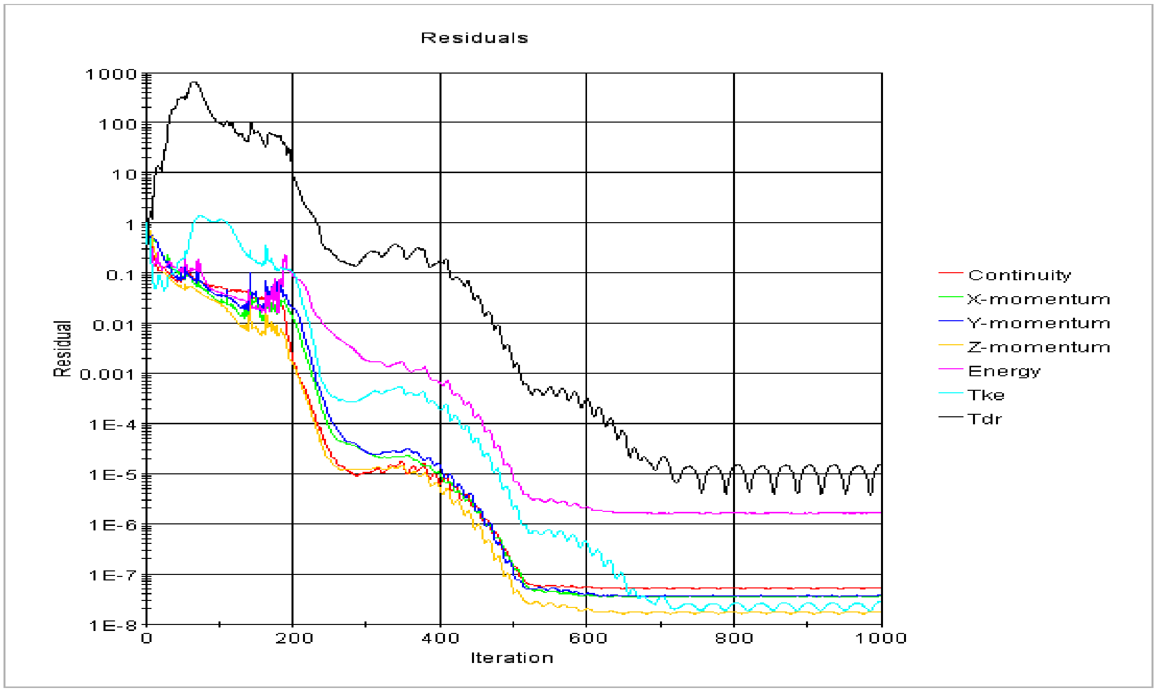

Figure 6.1: Residual plot for simulation at 30 kW for Hottest Channel